Spin reorientation driven by the interplay between spin-orbit coupling and Hund's rule coupling in iron pnictides

Morten H. Christensen, Jian Kang, Brian M. Andersen, Ilya Eremin, and Rafael M. Fernandes

Phys. Rev. B **92**, 214509 — Published 14 December 2015
DOI: 10.1103/PhysRevB.92.214509

Spin reorientation driven by the interplay between spin-orbit coupling and Hund's rule coupling in iron pnictides

Morten H. Christensen,[1, 2] Jian Kang,[1] Brian M. Andersen,[2] Ilya Eremin,[3, 4] and Rafael M. Fernandes[1]
[1]*School of Physics and Astronomy, University of Minnesota, Minneapolis, MN 55455, USA*
[2]*Niels Bohr Institute, University of Copenhagen, DK-2100, Denmark*
[3]*Institut für Theoretische Physik III, Ruhr-Universität Bochum, 44801 Bochum, Germany*
[4]*National University of Science and Technology 'MISiS', 119049 Moscow, Russian Federation*

In most magnetically-ordered iron pnictides, the magnetic moments lie in the FeAs planes, parallel to the modulation direction of the spin stripes. However, recent experiments in hole-doped iron pnictides have observed a reorientation of the magnetic moments from in-plane to out-of-plane. Interestingly, this reorientation is accompanied by a change in the magnetic ground state from a stripe antiferromagnet to a tetragonal non-uniform magnetic configuration. Motivated by these recent observations, here we investigate the origin of the spin anisotropy in iron pnictides using an itinerant microscopic electronic model that respects all the symmetry properties of a single FeAs plane. We find that the interplay between the spin-orbit coupling and the Hund's rule coupling can account for the observed spin anisotropies, including the spin reorientation in hole-doped pnictides, without the need to invoke orbital or nematic order. Our calculations also reveal an asymmetry between the magnetic ground states of electron- and hole-doped compounds, with only the latter displaying tetragonal magnetic states.

I. INTRODUCTION

In the iron pnictides, unconventional superconductivity appears in close proximity to a magnetic instability [1–4]. As a result, much of the research into these compounds has been devoted to understanding the magnetic properties of these systems [5–8]. Experimentally, the spin-density wave (SDW) magnetic order of most iron pnictides has orthorhombic (C_2) symmetry and corresponds to stripes of parallel spins modulated either along the $\hat{\mathbf{x}}$ direction (i.e. ordering vector $\mathbf{Q}_1 = (\pi, 0)$ and staggered magnetic order parameter $\mathbf{M}_1$) or along the $\hat{\mathbf{y}}$ direction (i.e. ordering vector $\mathbf{Q}_2 = (0, \pi)$ and staggered magnetic order parameter $\mathbf{M}_2$), in the coordinate system of the Fe square lattice [5, 6]. Theoretically, this state has been described by a variety of approaches, from purely localized Heisenberg spins [9–13] to itinerant nesting-based scenarios [14–22] to hybrid models mixing local moments and itinerant carriers [8, 23–27]. Common to nearly all these approaches is the assumption that the magnetic degrees of freedom have an underlying $O(3)$ spin-rotational symmetry. From a phenomenological perspective, this implies that the magnetic free energy F_{mag} depends only on the absolute value of the magnetic order parameters, i.e. $F_{\text{mag}}\left(M_1^2, M_2^2\right)$ [28].

Despite the success of these approaches in describing many magnetic properties of the iron pnictides – such as the onset of a preemptive nematic transition [29] and the appearance of a tetragonal magnetic ground state [22] – there are important features that remain largely unaddressed. In particular, the $O(3)$ rotational symmetry of a free spin does not hold for a magnetic moment in a crystal. Instead, the symmetries of the underlying lattice induce anisotropies in spin space that may be significant [30]. Indeed, in most iron pnictides, the magnetic moments are observed to point parallel to the modulation vector of the stripes, i.e. $\mathbf{M}_i \parallel \mathbf{Q}_i$ [5, 6]. Attesting the significance of this spin anisotropy, a sizable spin gap of the order of 10 meV is also found at low temperatures deep in the magnetically ordered state [31–34]. Interestingly, recent experiments in hole-doped iron pnictides have reported a spin reorientation near optimal doping, in which the direction of the magnetic moments flip from in-plane to out-of-plane [35–38]. Remarkably, this spin reorientation takes place in a region of the phase diagram in which the magnetic ground state changes from stripe/orthorhombic to tetragonal.

Therefore, elucidating the origins of these spin anisotropies and their impact on the normal state properties is paramount to advance our understanding of the iron pnictides. A natural candidate to account for these effects is the spin-orbit coupling (SOC) term $\lambda \mathbf{S} \cdot \mathbf{L}$ [39–42], which converts the lattice anisotropies into anisotropies in spin space. Recent ARPES measurements of the SOC λ have reported values of the order of 20 meV [43], which is not far from the typical magnetic energy scale of the problem (as extracted for instance from optical conductivity measurements [44, 45]). To include the SOC term in theoretical models, it is necessary to account for the puckering of the As atoms along the FeAs plane, which effectively doubles the unit cell of the Fe-only square lattice. In this paper, instead of working with the cumbersome ten-band model relevant for the 2-Fe unit cell, we consider a simpler low-energy microscopic model that respects all the symmetries of the FeAs plane and focuses only on the states near the Fermi level. Such a model, which relies on the smallness of the Fermi surface pockets of the iron pnictides, was previously derived by Cvetkovic and Vafek using rigorous group theoretical arguments [39]. Here, we show how the main ingredients of the model can be derived from a straightforward expansion of the usual five-orbital model for the pnictides. By computing microscopically the magnetic free energy in the paramagnetic state, we find the leading-order magnetic anisotropic terms:

$$\begin{aligned}\delta F = &\alpha_1 \left(M_{1,x}^2 + M_{2,y}^2\right) \\ &+\alpha_2 \left(M_{1,y}^2 + M_{2,x}^2\right) \\ &+\alpha_3 \left(M_{1,z}^2 + M_{2,z}^2\right) .\end{aligned} \tag{1}$$

The anisotropic coefficients α_i are proportional not only to the square of the SOC term, λ^2, but also to the Hund's rule coupling J. Evaluation of the coefficients reveals that $\alpha_1 < \alpha_3, \alpha_2$ for most of the temperature-doping phase diagram, implying that the magnetic moments have a general tendency to lie in the plane. Interestingly, in the hole-doped side of the phase diagram, we find a small region in which $\alpha_3 < \alpha_1, \alpha_2$, indicating a spin reorientation from in-plane to out-of-plane. Both results are in qualitative agreement with the observations discussed above, providing evidence that the SOC term, with the aid of the Hund's rule coupling, is sufficient to account for the magnetic anisotropies of the iron pnictides. This conclusion contrasts with previous proposals that orbital and/or nematic order are necessary to explain the observed magnetic moment orientation [30].

For completeness, we also analyze the nature of the magnetic ground state across the phase diagram. We find a general tendency of electron-doped compounds to form an orthorhombic uniaxial (single-$\mathbf{Q}$) stripe state (i.e. either $\langle|\mathbf{M}_1|\rangle = 0$ or $\langle|\mathbf{M}_2|\rangle = 0$), whereas hole-doped compounds favor a tetragonal biaxial (double-$\mathbf{Q}$) magnetic state (i.e. $\langle|\mathbf{M}_1|\rangle = \langle|\mathbf{M}_2|\rangle$). Such an electron-hole asymmetry is also qualitatively consistent with experiments – and in particular with the recent observation that the spin reorientation takes place in a region of the phase diagram in which the magnetic ground state is tetragonal.

The paper is organized as follows: In section II we introduce the low-energy microscopic model with the SOC term and the electronic interactions. Section III is devoted to the analysis of the coefficients of the free energy responsible for the magnetic anisotropy within leading-order. In section IV we refine the phase diagram by including fourth order contributions to the free energy that allow us to distinguish between stripe and tetragonal magnetic ground states. Concluding remarks are presented in section V. Details of the calculations are included in four appendices.

II. LOW-ENERGY MICROSCOPIC MODEL

We start with a low-energy microscopic model that focuses only on the electronic states near the Fermi level, while respecting the symmetries of the FeAs plane. Such a model was originally derived in Ref. [39] using the symmetry properties of the non-symmorphic space group $P4/nmm$ of a single FeAs plane. Here, we present an alternative derivation based on the typical 5-orbital tight-binding model used for the iron pnictides [46]:

$$\mathcal{H}_0 = \sum_{\mathbf{k}\mu\nu\alpha} \varepsilon_{\mu\nu}\left(\mathbf{k}\right) c_{\mu,\mathbf{k}\alpha}^{\dagger} c_{\nu,\mathbf{k}\alpha} \tag{2}$$

where $\mathbf{k}$ is the momentum, α is the spin, and μ, ν denote one of the five Fe orbitals, xz, yz, $x^2 - y^2$, xy, and $3z^2 - r^2$. The matrix $\varepsilon_{\mu\nu}\left(\mathbf{k}\right)$ corresponds to the Fourier-transformed tight-binding dispersions involving up to fourth-nearest neighbor hoppings. Its explicit expression is given in Appendix A. Note that this Hamiltonian is based on the single-Fe square lattice (i.e. it refers to the "unfolded" Brillouin zone), and that the coordinate system is defined such that k_x and k_y are parallel to the nearest-neighbor Fe atoms directions. The actual crystallographic unit cell contains two Fe atoms due to the puckering of the As atoms, resulting in the so-called "folded" Brillouin zone, described by the coordinates K_x, K_y (see Fig. 1). Note that the two coordinate systems are related by:

$$\begin{aligned}K_x &= k_x + k_y \\ K_y &= -k_x + k_y\end{aligned} \tag{3}$$

where the momentum in the unfolded zone is measured in units of its inverse lattice constant $1/a$, whereas the momentum in the folded zone is measured in units of the its inverse lattice constant $1/\left(\sqrt{2}a\right)$.

The key properties that allow us to derive a simpler low-energy model are the facts that the Fermi surface pockets are small and that the orbitals that mostly contribute to the Fermi surface are xz, yz, xy. In particular, the idea is to start at the high-symmetry points of the unfolded Brillouin zone (namely, $\Gamma = (0, 0)$, $X = (\pi, 0)$, and $Y = (0, \pi)$), where the band states are pure orbital states, and perform an expansion of the corresponding matrix elements $\varepsilon_{\mu\nu}\left(\mathbf{k}\right)$ for small momentum. Note that, to focus on a general and analytically tractable model, we follow Ref. [39] and ignore the states near the (π, π) point of the unfolded Brillouin zone. While it is true that some iron pnictides display a hole-pocket with xy-orbital character centered at this point, this pocket is not usually present for all values of k_z, and is absent in many of the iron-based materials with a single FeAs plane per unit cell. Correspondingly we consider in this work the doping range in which this pocket lies below the Fermi level.

Consider first the Γ point; the two states closest to the Fermi level are the xz and yz orbitals, which form a degenerate doublet in the absence of SOC. Thus, for small $\mathbf{k}$, we define the spinor:

$$\psi_{\Gamma,\mathbf{k}} = \begin{pmatrix} c_{yz,\mathbf{k}\uparrow} \\ -c_{xz,\mathbf{k}\uparrow} \\ c_{yz,\mathbf{k}\downarrow} \\ -c_{xz,\mathbf{k}\downarrow} \end{pmatrix} . \tag{4}$$

Projecting $\varepsilon_{\mu\nu}\left(\mathbf{k}\right)$ on this sub-space and expanding for small $\mathbf{k}$ then yields the 4×4 Hamiltonian:

$$H_{0,\Gamma} = \sum_{\mathbf{k}} \psi_{\Gamma,\mathbf{k}}^{\dagger} h_{\Gamma}\left(\mathbf{k}\right) \psi_{\Gamma,\mathbf{k}} \tag{5}$$

with

$$h_\Gamma(\mathbf{k}) = \begin{pmatrix} \epsilon_\Gamma + 2\frac{\mathbf{k}^2}{2m_\Gamma} + b\left(k_x^2 - k_y^2\right) & 4ck_xk_y \\ 4ck_xk_y & \epsilon_\Gamma + 2\frac{\mathbf{k}^2}{2m_\Gamma} - b\left(k_x^2 - k_y^2\right) \end{pmatrix} \otimes \sigma^0 \qquad (6)$$

where σ^0 is a Pauli matrix acting on spin space. The coefficients ϵ_Γ, m_Γ, b, and c can be obtained directly from the tight-binding parameters (see Appendix A). Note, however, that as we move away from the high-symmetry points of the Brillouin zone, other orbitals start to contribute to the electronic states. Consequently, the coefficients of the expansion (as derived in Appendix A) will be slightly renormalized by the hybridization with the orbitals not included in the expansion, although the form of the expansion remains invariant. To account for this issue, we can consider the coefficients to be free parameters that can be fit directly to the first-principle band dispersions.

Near the X point, the low-energy states correspond to the orbitals yz and xy. Defining the spinor:

$$\psi_{X,\mathbf{k}+\mathbf{Q}_1} = \begin{pmatrix} c_{yz,\mathbf{k}+\mathbf{Q}_1\uparrow} \\ c_{xy,\mathbf{k}+\mathbf{Q}_1\uparrow} \\ c_{yz,\mathbf{k}+\mathbf{Q}_1\downarrow} \\ c_{xy,\mathbf{k}+\mathbf{Q}_1\downarrow} \end{pmatrix}. \qquad (7)$$

and expanding the projected $\varepsilon_{\mu\nu}(\mathbf{k})$ near $\mathbf{Q}_1 = (\pi, 0)$ yields:

$$H_{0,X} = \sum_{\mathbf{k}} \psi^\dagger_{X,\mathbf{k}+\mathbf{Q}_1} h_X\left(\mathbf{k}+\mathbf{Q}_1\right) \psi_{X,\mathbf{k}+\mathbf{Q}_1} \qquad (8)$$

with

$$h_X(\mathbf{k}+\mathbf{Q}_1) = \begin{pmatrix} \epsilon_1 + 2\frac{\mathbf{k}^2}{2m_1} + a_1\left(k_x^2 - k_y^2\right) & -iv_X(\mathbf{k}) \\ iv_X(\mathbf{k}) & \epsilon_3 + 2\frac{\mathbf{k}^2}{2m_3} + a_3\left(k_x^2 - k_y^2\right) \end{pmatrix} \otimes \sigma^0 \qquad (9)$$

and:

$$v_X(\mathbf{k}) = 2vk_y + 2p_1k_y(k_y^2 + 3k_x^2) - 2p_2k_y(k_x^2 - k_y^2). \qquad (10)$$

Similarly, near the Y point, the low-energy states involve the orbitals xz and xy:

$$\psi_{Y,\mathbf{k}+\mathbf{Q}_2} = \begin{pmatrix} c_{xz,\mathbf{k}+\mathbf{Q}_2\uparrow} \\ c_{xy,\mathbf{k}+\mathbf{Q}_2\uparrow} \\ c_{xz,\mathbf{k}+\mathbf{Q}_2\downarrow} \\ c_{xy,\mathbf{k}+\mathbf{Q}_2\downarrow} \end{pmatrix}. \qquad (11)$$

Projecting and expanding $\varepsilon_{\mu\nu}(\mathbf{k})$ near $\mathbf{Q}_2 = (0, \pi)$ gives:

$$H_{0,Y} = \sum_{\mathbf{k}} \psi^\dagger_{Y,\mathbf{k}+\mathbf{Q}_2} h_Y\left(\mathbf{k}+\mathbf{Q}_2\right) \psi_{Y,\mathbf{k}+\mathbf{Q}_2} \qquad (12)$$

with

$$h_Y(\mathbf{k}+\mathbf{Q}_2) = \begin{pmatrix} \epsilon_1 + 2\frac{\mathbf{k}^2}{2m_1} - a_1\left(k_x^2 - k_y^2\right) & -iv_Y(\mathbf{k}) \\ iv_Y(\mathbf{k}) & \epsilon_3 + 2\frac{\mathbf{k}^2}{2m_3} - a_3\left(k_x^2 - k_y^2\right) \end{pmatrix} \otimes \sigma^0 \qquad (13)$$

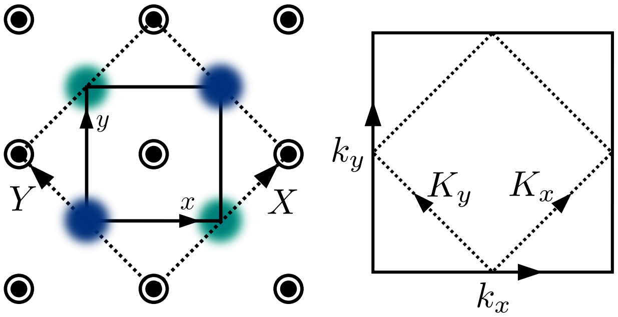

FIG. 1. (Color online) (Left) Illustration of the 2-Fe (dotted line) and 1-Fe (solid line) unit cells. The black dots denote iron atoms, while the pnictogens form two sublattices, one above the iron-plane (dark blue) and one below the iron-plane (light blue). (Right) Brillouin zones corresponding to the 1-Fe and 2-Fe unit cells. The dotted line is the "folded" Brillouin zone, corresponding to the 2-Fe unit cell, while the solid line is the "unfolded" Brillouin zone, corresponding to the 1-Fe unit cell.

and:

$$v_Y(\mathbf{k}) = -2vk_x - 2p_1k_x(k_x^2 + 3k_y^2) - 2p_2k_x(k_x^2 - k_y^2). \qquad (14)$$

Having established the low-energy states in the unfolded Brillouin zone (i.e. the one referring to the 1-Fe unit cell), it is now straightforward to fold the states into the 2-Fe unit cell (see Fig. 1). Despite working in the folded Brillouin zone, described by the coordinates K_x, K_y, we will still make use of the coordinates k_x, k_y of the unfolded zone. From Eq. (3), we find that upon folding, both momenta $\mathbf{Q}_1 = (\pi, 0)$ and $\mathbf{Q}_2 = (0, \pi)$ are identified with the same momentum $\mathbf{Q}_M = (\pi, \pi)$. It is straightforward to show that the spinors X and Y now combine to form two new degenerate doublets at the $M = (\pi, \pi)$ point of the folded zone:

$$\psi_{M_1,\mathbf{k}+\mathbf{Q}_M} = \begin{pmatrix} c_{xz,\mathbf{k}+\mathbf{Q}_2\uparrow} \\ c_{yz,\mathbf{k}+\mathbf{Q}_1\uparrow} \\ c_{xz,\mathbf{k}+\mathbf{Q}_2\downarrow} \\ c_{yz,\mathbf{k}+\mathbf{Q}_1\downarrow} \end{pmatrix}; \psi_{M_3,\mathbf{k}+\mathbf{Q}_M} = \begin{pmatrix} c_{xy,\mathbf{k}+\mathbf{Q}_2\uparrow} \\ c_{xy,\mathbf{k}+\mathbf{Q}_1\uparrow} \\ c_{xy,\mathbf{k}+\mathbf{Q}_2\downarrow} \\ c_{xy,\mathbf{k}+\mathbf{Q}_1\downarrow} \end{pmatrix} \qquad (15)$$

Hereafter, we will consider the momentum of any spinor as measured relative to the high-symmetry points, as appropriate. Then, the non-interacting Hamiltonian becomes:

$$\mathcal{H}_0 = \sum_{\mathbf{k}} \Psi^\dagger_{\mathbf{k}} \left[H_0(\mathbf{k}) - \mu\mathbb{1}\right] \Psi_{\mathbf{k}}, \qquad (16)$$

where we defined the enlarged spinor:

$$\Psi_{\mathbf{k}} = \begin{pmatrix} \psi_{Y,\mathbf{k}} \\ \psi_{X,\mathbf{k}} \\ \psi_{\Gamma,\mathbf{k}} \end{pmatrix} \qquad (17)$$

and the Hamiltonian matrix:

$$H_0(\mathbf{k}) = \begin{pmatrix} h_Y(\mathbf{k}) & 0 & 0 \\ 0 & h_X(\mathbf{k}) & 0 \\ 0 & 0 & h_\Gamma(\mathbf{k}) \end{pmatrix} \qquad (18)$$

where μ is the chemical potential and $\mathbb{1}$ is the identity matrix. We note that this model has the same properties of the Hamiltonian derived by Cvetkovic and Vafek in Ref. [39] combining a $\mathbf{k}\cdot\mathbf{p}$ expansion and the symmetry properties of the $P4/nmm$ space group (note, however, that the definition of the spinors X and Y are switched in Ref. [39] with respect to the notation adopted here). In the group-theory language, the spinor ψ_Γ belongs to the two-dimensional E_g representation of $P4/nmm$ near the Γ point, whereas ψ_{M_1} and ψ_{M_3} belong to the two-dimensional E_{M_1} and E_{M_3} representations of $P4/nmm$ near the M point. Hereafter, we will use for the coefficients of the Hamiltonian the parameters given by Table IX in Ref. [39]. Those were obtained by direct fitting of the band dispersions to first-principle calculations. The resulting band dispersions, as well as the Fermi surface, are shown in Fig. 2. Note also that this low-energy model is fundamentally different than two-orbital models that restrict the Hamiltonian to the subspace of the xz and yz orbitals. Our model, derived from the five-orbital tight-binding model as shown in Appendix A, not only obeys all the symmetries imposed by the $P4/nmm$ space group, but it also contains information about all the orbitals that contribute to the Fermi surface, including the xy orbital.

Besides the band dispersions, the non-interacting Hamiltonian must also contain the SOC term $\lambda\mathbf{S}\cdot\mathbf{L}$, with $\mathbf{S}$ denoting the spin angular momentum operator and $\mathbf{L}$, the orbital angular momentum operator. Note that this atomic-like term preserves the Kramers degeneracy of each state. To proceed, we project this term from the $L=2$ cubic harmonic basis to the orbital basis (see Appendix B for more details). At the Γ point, we obtain an admixture of the xz and yz orbitals:

$$\frac{\lambda}{2}\sum_{\mathbf{k}\alpha\beta}\left(ic^\dagger_{yz,\mathbf{k}\alpha}\sigma^z_{\alpha\beta}c_{xz,\mathbf{k}\beta}+\text{h.c.}\right)= \frac{\lambda}{2}\sum_{\mathbf{k}}\psi^\dagger_{\Gamma,\mathbf{k}}\left(\tau^y\otimes\sigma^z\right)\psi_{\Gamma,\mathbf{k}} \qquad (19)$$

where, in the last step, we used the definition of the spinors. At the M point, we obtain the admixture of xz/yz and xy orbitals:

$$\frac{\lambda}{2}\sum_{\mathbf{k}\alpha\beta}\left(ic^\dagger_{xz,\mathbf{k}\alpha}\sigma^x_{\alpha\beta}c_{xy,\mathbf{k}\beta}+\text{h.c.}\right)= \frac{\lambda}{2}\sum_{\mathbf{k}}\left[i\psi^\dagger_{Y,\mathbf{k}+\mathbf{Q_2}}\left(\tau^+\otimes\sigma^x\right)\psi_{X,\mathbf{k}+\mathbf{Q_1}}+\text{h.c.}\right] \qquad (20)$$

as well as:

$$\frac{\lambda}{2}\sum_{\mathbf{k}\alpha\beta}\left(ic^\dagger_{xy,\mathbf{k}\alpha}\sigma^y_{\alpha\beta}c_{yz,\mathbf{k}\beta}+\text{h.c.}\right)= \frac{\lambda}{2}\sum_{\mathbf{k}}\left[i\psi^\dagger_{Y,\mathbf{k}+\mathbf{Q_2}}\left(\tau^-\otimes\sigma^y\right)\psi_{X,\mathbf{k}+\mathbf{Q_1}}+\text{h.c.}\right] \qquad (21)$$

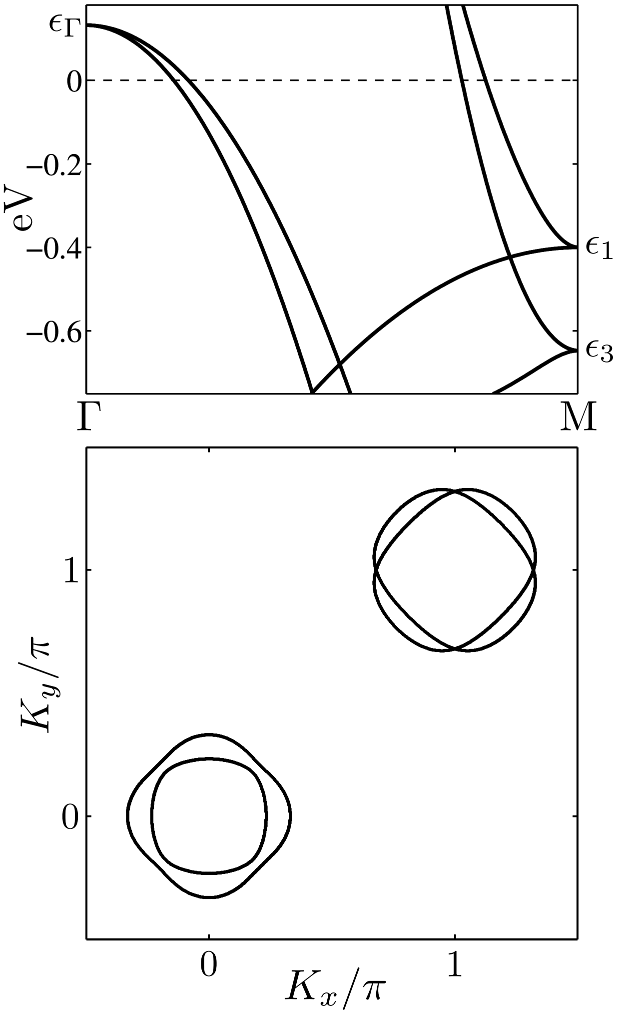

FIG. 2. (upper panel) Cut of the low-energy band dispersion from the $\Gamma=(0,0)$ to the $M=(\pi,\pi)$ point of the folded Brillouin zone with parameters fit to the tight-binding model of Ref. [47]. The corresponding Fermi surface is shown in the lower panel.

with $\tau^\pm=\frac{1}{2}\left(\tau^x\pm i\tau^y\right)$. Therefore, the SOC becomes:

$$\mathcal{H}_{\text{SOC}}=\sum_{\mathbf{k}}\Psi^\dagger_{\mathbf{k}}H_{\text{SOC}}(\mathbf{k})\Psi_{\mathbf{k}}\,, \qquad (22)$$

with:

$$H_{\text{SOC}}(\mathbf{k})=\begin{pmatrix}0 & h^{\text{SOC}}_M(\mathbf{k}) & 0\\ \left(h^{\text{SOC}}_M(\mathbf{k})\right)^\dagger & 0 & 0\\ 0 & 0 & h^{\text{SOC}}_\Gamma(\mathbf{k})\end{pmatrix} \qquad (23)$$

such that:

$$h^{\text{SOC}}_\Gamma(\mathbf{k})=\frac{1}{2}\lambda\left(\tau^y\otimes\sigma^z\right)\,, \qquad (24)$$

$$h^{\text{SOC}}_M(\mathbf{k})=\frac{i}{2}\lambda\left(\tau^+\otimes\sigma^x+\tau^-\otimes\sigma^y\right)\,, \qquad (25)$$

in agreement with the group-theoretical arguments of Ref. [39].

The interacting part of this low-energy model is rather complex, involving 30 different possible biquadratic terms in the fermionic operators. Here, we will focus on the interactions coupling the Γ and the M points, since those are the ones that will be relevant for the calculation of the magnetic action in the next section. Defining $\tilde{\tau}^{1,3} \equiv \frac{1}{2}(\tau^0 \pm \tau^z)$, the interacting terms coupling the Γ and M points are written as (see Ref. [39]):

$$\begin{aligned}\mathcal{H}_{\text{int}} = \frac{1}{2}\sum_{\mathbf{k}\sigma} \Big[& v_{13}\left(\psi^{\dagger}_{X\sigma}(\mathbf{k})\tau^{-}\psi_{\Gamma\sigma}(\mathbf{k}) + \text{h.c.}\right)^2 \\ & + v_{13}\left(\psi^{\dagger}_{Y\sigma}(\mathbf{k})\tilde{\tau}^{3}\psi_{\Gamma\sigma}(\mathbf{k}) + \text{h.c.}\right)^2 \\ & + v_{15}\left(\psi^{\dagger}_{X\sigma}(\mathbf{k})\tilde{\tau}^{3}\psi_{\Gamma\sigma}(\mathbf{k}) + \text{h.c.}\right)^2 \\ & + v_{15}\left(\psi^{\dagger}_{Y\sigma}(\mathbf{k})\tau^{-}\psi_{\Gamma\sigma}(\mathbf{k}) + \text{h.c.}\right)^2 \\ & + v_{17}\left(\psi^{\dagger}_{X\sigma}(\mathbf{k})\tau^{+}\psi_{\Gamma\sigma}(\mathbf{k}) + \text{h.c.}\right)^2 \\ & + v_{17}\left(\psi^{\dagger}_{Y\sigma}(\mathbf{k})\tilde{\tau}^{1}\psi_{\Gamma\sigma}(\mathbf{k}) + \text{h.c.}\right)^2 \\ & + v_{19}\left(\psi^{\dagger}_{X\sigma}(\mathbf{k})\tilde{\tau}^{1}\psi_{\Gamma\sigma}(\mathbf{k}) + \text{h.c.}\right)^2 \\ & + v_{19}\left(\psi^{\dagger}_{Y\sigma}(\mathbf{k})\tau^{+}\psi_{\Gamma\sigma}(\mathbf{k}) + \text{h.c.}\right)^2 \Big], \end{aligned} \tag{26}$$

Note that all terms are diagonal in spin space. In terms of the more usual multi-orbital Hubbard model with on-site interactions, the first three coefficients originate from the Hund's rule coupling, $v_{13} = v_{15} = v_{17} = J$, while the last one arises from the intra-orbital Hubbard term, $v_{19} = U/2$ [39]. Here, we are not interested in which interactions will drive the SDW transition. Rather, we will assume a nearby SDW instability and compute how the interplay between these interactions and the SOC affect the magnetic action.

Finally, in order to be able to derive the magnetic action in the next sections, we need also to establish how the magnetic order parameters $\mathbf{M}_1$ and $\mathbf{M}_2$, corresponding to $(\pi, 0)$ and $(0, \pi)$ order in the unfolded zone, couple to the low-energy electronic states. Here, we will consider only intra-orbital magnetism. Indeed, previous Hartree-Fock investigations of the five-orbital Hubbard model have shown that the dominant contributions to the magnetic instability arise from intra-orbital couplings [48, 49]. Therefore, the SDW vertices become:

$$\begin{aligned}\mathcal{H}_{\text{SDW}} = \mathbf{M}_1 \cdot & \sum_{\mathbf{k}\alpha\beta}\left(c^{\dagger}_{yz,\mathbf{k}\alpha}\boldsymbol{\sigma}_{\alpha\beta}c_{yz,\mathbf{k}+\mathbf{Q}_1\beta} + \text{h.c.}\right) \\ + \mathbf{M}_2 \cdot & \sum_{\mathbf{k}\alpha\beta}\left(c^{\dagger}_{xz,\mathbf{k}\alpha}\boldsymbol{\sigma}_{\alpha\beta}c_{xz,\mathbf{k}+\mathbf{Q}_2\beta} + \text{h.c.}\right)\end{aligned} \tag{27}$$

which, transformed to the spinor representation, yields:

$$\begin{aligned}\mathcal{H}_{\text{SDW}} = \mathbf{M}_1 \cdot & \sum_{\mathbf{k}}\left[\psi^{\dagger}_{\Gamma,\mathbf{k}}\left(\tilde{\tau}^1 \otimes \boldsymbol{\sigma}\right)\psi_{X,\mathbf{k}+\mathbf{Q}_1} + \text{h.c.}\right] \\ + \mathbf{M}_2 \cdot & \sum_{\mathbf{k}}\left[\psi^{\dagger}_{\Gamma,\mathbf{k}}\left(-\tau^{-} \otimes \boldsymbol{\sigma}\right)\psi_{Y,\mathbf{k}+\mathbf{Q}_1} + \text{h.c.}\right]\end{aligned} \tag{28}$$

Note that, in the language of Ref. [39], the SDW Hamiltonian transforms under the E_{M_4} two-dimensional irreducible representation of $P4/nmm$.

III. ANISOTROPIC MAGNETIC FREE ENERGY

To understand the origin of the magnetic anisotropies, we first review the group theoretical arguments of Ref. [39]. In the absence of SOC, all the components of the magnetic order parameters belong to the same irreducible representation E_{M_4}, as shown above, and the free energy depends only on the invariant form $\mathbf{M}_1^2 + \mathbf{M}_2^2$. However, with the introduction of SOC, the spin and orbital degrees of freedom are no longer independent. Consequently, the components of $\mathbf{M}_i$ must belong to different irreducible representations of $P4/nmm$, if one enforces the combination of the spin *and* orbital parts of the magnetic order parameter to still transform under E_{M_4}. As a result, the individual components of $\mathbf{M}_1$ and $\mathbf{M}_2$ transform according to the following two-dimensional irreducible representations [39]

$$E_{M_1}: \begin{pmatrix} M_{1,x} \\ M_{2,y} \end{pmatrix} \quad E_{M_2}: \begin{pmatrix} M_{1,y} \\ M_{2,x} \end{pmatrix} \quad E_{M_3}: \begin{pmatrix} M_{1,z} \\ M_{2,z} \end{pmatrix} \tag{29}$$

Because these components belong to different irreducible representations, they will, in general, have different transition temperatures. Therefore, the free energy must acquire the leading-order anisotropic terms:

$$\begin{aligned}\delta F = \alpha_1 & \left(M_{1,x}^2 + M_{2,y}^2\right) \\ + \alpha_2 & \left(M_{1,y}^2 + M_{2,x}^2\right) \\ + \alpha_3 & \left(M_{1,z}^2 + M_{2,z}^2\right) .\end{aligned} \tag{30}$$

The smallest α_i coefficient determines which type of magnetic order condenses first. In Fig. 3, we show separately the real-space spin configurations corresponding to the components of $\mathbf{M}_1$ and $\mathbf{M}_2$ associated with each coefficient α_i. Specifically, if $\alpha_1 < \alpha_2, \alpha_3$, then $\mathbf{M}_i$ points parallel to the ordering vector $\mathbf{Q}_i$ (of the unfolded zone); if $\alpha_2 < \alpha_1, \alpha_3$, $\mathbf{M}_i$ still points in-plane, but perpendicular to the ordering vector $\mathbf{Q}_i$. Finally, if $\alpha_3 < \alpha_1, \alpha_2$, $\mathbf{M}_i$ points out-of-plane. Note that this analysis does not reveal whether only either $\mathbf{M}_1$ or $\mathbf{M}_2$ condense, or if both condense simultaneously. To establish the actual ground state, it is necessary to go to higher order in the free energy. We will come back to this point in Section IV. Note that the spin-anisotropic terms preserve the tetragonal symmetry of the system.

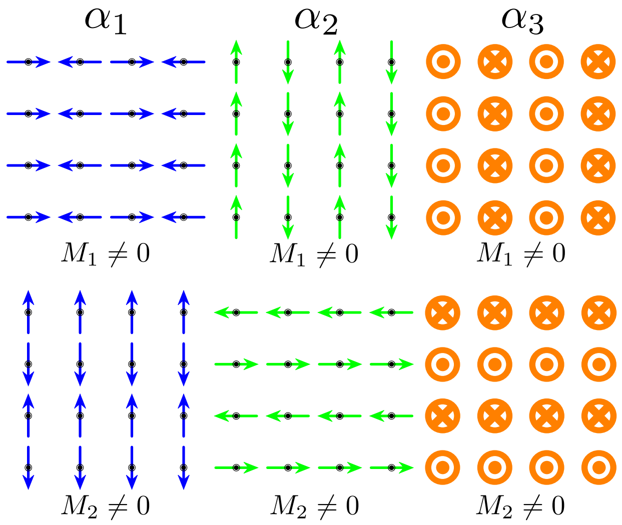

FIG. 3. Sketch of the different uniaxial (i.e. stripe-like) magnetic configurations corresponding to the different anisotropic terms in the magnetic free energy (30) with coefficients α_1, α_2, and α_3.

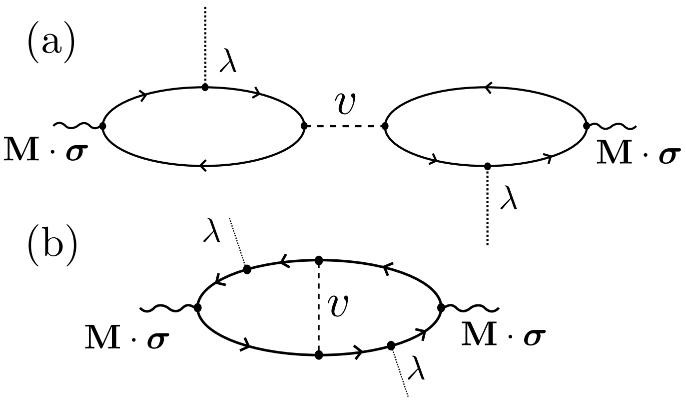

FIG. 4. Schematic representation of the two distinct type of Feynman diagrams at $\mathcal{O}(v, \lambda^2)$: two-loop diagrams (a) and one-loop diagrams (b). Only the one-loop diagrams contribute to the anisotropic terms.

Here, our goal is to evaluate microscopically the α_i coefficients using the model of the previous section. Within the non-interacting part of the model, we find that even the presence of spin-orbit coupling does not introduce magnetic anisotropies. The reason is that the model effectively has an enlarged $P4/nmm \otimes P4/nmm$ symmetry, since the states at Γ and the states at M are treated independently. Of course, the fact that these states are connected in realistic tight-binding models ensures that some level of spin-anisotropy will be introduced at the non-interacting level. Such an effect will be likely a high-energy effect, as it involves states away from the Fermi level [50]. Here, instead, we focus on the low-energy contributions to the spin anisotropy. Consequently, they must come from interactions – particularly, from the interaction terms that couple the states at Γ and at M, and therefore remove the enlarged $P4/nmm \otimes P4/nmm$ symmetry. These are precisely the terms listed in Eq. (26).

We proceed with a straightforward diagrammatic approach by dressing the non-interacting particle-hole bubble with the SOC term λ in Eq. (23) and with the interactions v_i in Eq. (26). The SDW vertices coupling the magnetic order parameters to the non-interacting Green's functions are those derived in Eq. (28). Both λ and v_i are treated perturbatively to leading order. Because terms of the order $\mathcal{O}(\lambda)$ are forbidden by symmetry, we consider the diagrams of the orders $\mathcal{O}(\lambda^2)$ and $\mathcal{O}(v_i)$.

To order $\mathcal{O}(v_i)$, there are two distinct types of interaction-dressed diagrams, as depicted in Fig. 4. On top of that, to order $\mathcal{O}(\lambda^2)$, each of the two diagrams can be dressed by a pair of SOC legs in eight different ways. Because symmetry requirements forbid terms that couple directly $\mathbf{M}_1$ and $\mathbf{M}_2$ at the quadratic level, the pair of SOC legs must correspond to the same SOC term, i.e. either $h_{\Gamma}^{\mathrm{SOC}}(\mathbf{k})$ or $h_{M}^{\mathrm{SOC}}(\mathbf{k})$ in Eq. (23). Explicit calculation of the traces over the Pauli-matrices reveals also that the only combinations of SOC legs that yield anisotropic magnetic terms are those in which one SOC leg appears in the upper-right (lower-right) part of the diagram and the other SOC leg appears in the lower-left (upper-left) part of the diagram.

We find that all two-loop diagrams (i.e. those represented in Fig. 4a) vanish, and therefore do not contribute to the magnetic anisotropy term (30). We show this explicitly in Appendix C. Therefore, all that is left is to compute the one-loop diagram represented in Fig. 4b. The calculation is tedious but straightforward. To illustrate it, consider the interaction v_{13}. The one-loop diagrams contributing to the anisotropic terms $M_{1,\mu}^2$ are shown in Fig. 5. As mentioned above, there are two possible placements for the two SOC legs, in opposite sides of the loop. For each diagram, one has to also consider its hermitian-conjugate partner, since the interaction vertices and the SDW vertices are not adjoint operators. Furthermore, the diagrammatic rules derived for this problem impose an overall minus sign to each one-loop diagram, and enforce the trace over the Pauli matrices to be taken in the direction opposite to the arrows. Finally, to compute these traces, it is useful to employ the following Pauli matrix identity:

$$\mathrm{tr}\left(\sigma^i \sigma^j \sigma^k \sigma^l\right) = 2\left(\delta^{ij}\delta^{kl} - \delta^{ik}\delta^{jl} + \delta^{il}\delta^{jk}\right) \qquad (31)$$

A straightforward evaluation of these four diagrams gives then three different anisotropic terms for the magnetic free energy:

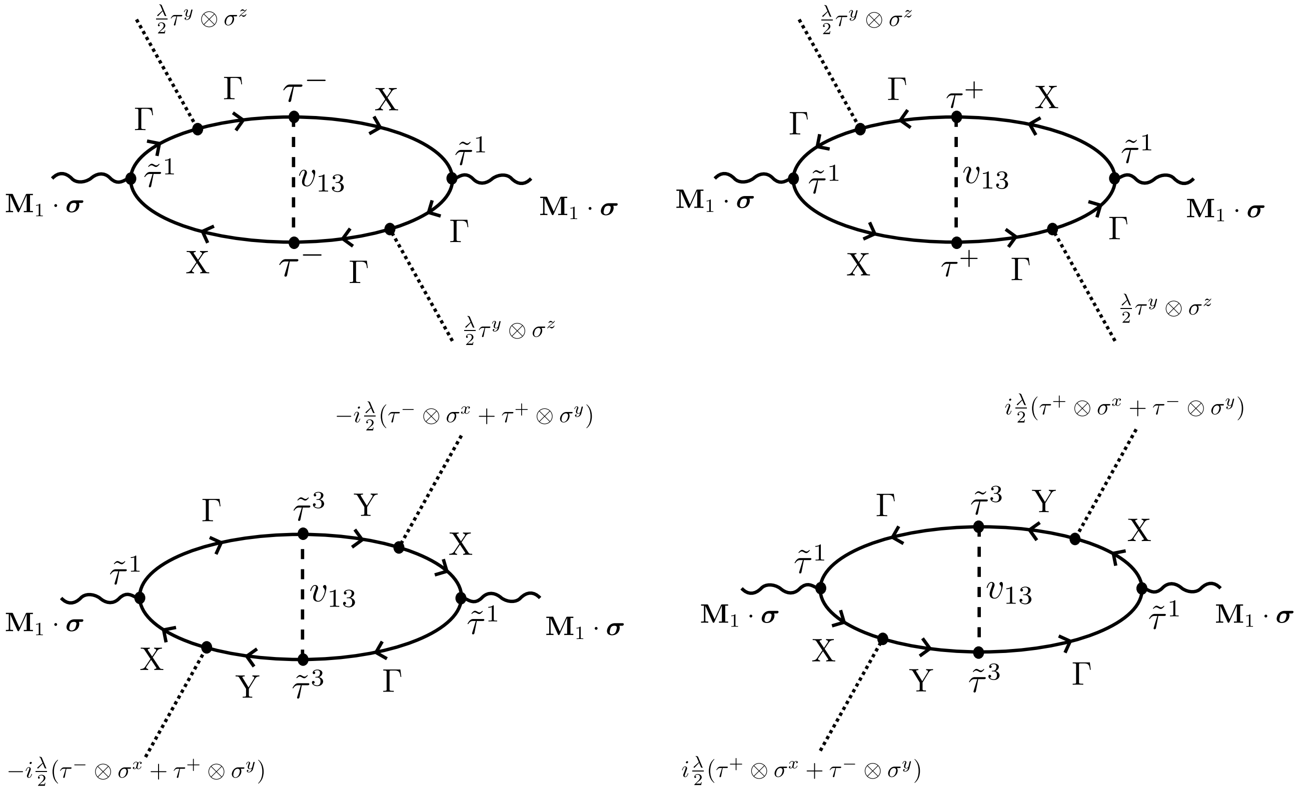

FIG. 5. Illustration of distinct second-order one-loop diagrams in the case where the electron-electron interaction is given by v_{13} and the magnetic order parameter is $\mathbf{M}_1$. Note that the electron-electron vertex depends on the direction of momentum, i.e. the upper left and upper right diagrams are not identical.

$$\begin{aligned}
\delta F = -v_{13}\frac{\lambda^2}{2} \sum_{\substack{\mathbf{k}\mathbf{k}' \\ \omega_n\omega_{n'}}} &\Big(\mathrm{tr}\left(\tilde{\tau}^1 G'_X \tau^- G'_\Gamma \tau^y G'_\Gamma \tilde{\tau}^1 G_X \tau^- G_\Gamma \tau^y G_\Gamma\right) + \mathrm{tr}\left(\tilde{\tau}^1 G'_\Gamma \tau^y G'_\Gamma \tau_+ G'_X \tilde{\tau}^1 G_\Gamma \tau^y G_\Gamma \tau^+ G_X\right)\Big)\left(M_{1,z}^2 - M_{1,x}^2 - M_{1,y}^2\right) \\
+ \ v_{13}\frac{\lambda^2}{2} \sum_{\substack{\mathbf{k}\mathbf{k}' \\ \omega_n\omega_{n'}}} &\Big(\mathrm{tr}\left(\tilde{\tau}^1 G'_X \tau^- G'_Y \tilde{\tau}^3 G'_\Gamma \tilde{\tau}^1 G_X \tau^- G_Y \tilde{\tau}^3 G_\Gamma\right) + \mathrm{tr}\left(\tilde{\tau}^1 G'_\Gamma \tilde{\tau}^3 G'_Y \tau^+ G'_X \tilde{\tau}^1 G_\Gamma \tilde{\tau}^3 G_Y \tau^+ G_X\right)\Big)\left(M_{1,x}^2 - M_{1,y}^2 - M_{1,z}^2\right) \\
+ \ v_{13}\frac{\lambda^2}{2} \sum_{\substack{\mathbf{k}\mathbf{k}' \\ \omega_n\omega_{n'}}} &\Big(\mathrm{tr}\left(\tilde{\tau}^1 G'_X \tau^+ G'_Y \tilde{\tau}^3 G'_\Gamma \tilde{\tau}^1 G_X \tau^+ G_Y \tilde{\tau}^3 G_\Gamma\right) + \mathrm{tr}\left(\tilde{\tau}^1 G'_\Gamma \tilde{\tau}^3 G'_Y \tau^- G'_X \tilde{\tau}^1 G_\Gamma \tilde{\tau}^3 G_Y \tau^- G_X\right)\Big)\left(M_{1,y}^2 - M_{1,x}^2 - M_{1,z}^2\right) \\
\delta F \ = \ v_{13}\lambda^2 &\Big(\sum_{\mathbf{k},\omega_n} [G_X]_{12}[G_Y]_{12}[G_\Gamma]_{21}\Big)^2 \left(M_{1,x}^2 - M_{1,y}^2 - M_{1,z}^2\right) . \qquad (32)
\end{aligned}$$

Here, the primed Green's functions are short-handed notations for $G'_i = G_i\left(\mathbf{k}', \omega'_n\right)$. The Green functions are given by

$$[G_A]_{ij} = \sum_m \frac{a^i_m(\mathbf{k})_A a^j_m(\mathbf{k})^*_A}{i\omega_n - (\epsilon_{A,m}(\mathbf{k}) - \mu)} , \qquad (33)$$

where $\epsilon_{A,m}(\mathbf{k})$ are the eigenenergies of the matrix $h_A(\mathbf{k})$ and $a^i_m(\mathbf{k})_A$ is the unitary transformation between the spinor basis and the band basis. In Eq. (32), the coefficient of the term $\left(M_{1,z}^2 - M_{1,x}^2 - M_{1,y}^2\right)$ vanishes because of the antisymmetry of the $G_\Gamma \tau^y G_\Gamma$ matrix in spinor space, whereas the coefficient of $\left(M_{1,y}^2 - M_{1,x}^2 - M_{1,z}^2\right)$ vanishes because $[G_\Gamma]_{12}(\mathbf{k}) \propto k_x k_y$, causing the sum over momentum to vanish.

Note that while the upper diagrams shown in Fig. 5 introduce the anisotropy between the in-plane and out-of-plane components of the magnetic order parameter, the lower diagrams contribute to the anisotropy between $M_{1,x}$ and $M_{1,y}$. The reason for this is the character of the SOC in the effective model, which remains diagonal in the spin sector near the Γ-point due to xz- and yz-orbital characters of the electronic states. As a result, particle-hole excitations involving fermions from the $\Gamma-$point and from the X/Y-point do not allow for a spin-flip, which would be necessary to generate the anisotropy between $M_{1,x}$ and $M_{1,y}$. Only the inclusion of the particle-hole excitations between the two electron pockets, as described by the lower diagrams, generates the anisotropy between the x and y components of the magnetization.

Repeating the same calculation for $\mathbf{M}_2$ gives the same result, but with $M_{1,x} \to M_{2,y}$ and $M_{1,y} \to M_{2,x}$, as expected by symmetry. Therefore, we can recast this contribution to the free energy in the form of Eq. (30) via differences in the anisotropic coefficients α:

$$\alpha_2^{(v_{13})} - \alpha_1^{(v_{13})} = -2v_{13}\lambda_M^2 \Big(\sum_{\mathbf{k},\omega_n} [G_X]_{12}[G_Y]_{12}[G_\Gamma]_{21} \Big)^2 \quad (34)$$

$$\alpha_3^{(v_{13})} - \alpha_1^{(v_{13})} = 0\,. \quad (35)$$

The same procedure applied to the other interactions v_{15}, v_{17}, and v_{19} reveals that only the first two give rise to anisotropic terms. The final result for the anisotropic coefficients is:

$$\begin{aligned} \alpha_2 - \alpha_1 = {} & 2v_{15}\lambda^2 \Big(\sum_{\mathbf{k},\omega_n} [G_\Gamma]_{11}[G_X]_{11}[G_Y]_{22} \Big)^2 \\ & -2v_{13}\lambda^2 \Big(\sum_{\mathbf{k},\omega_n} [G_\Gamma]_{21}[G_X]_{12}[G_Y]_{12} \Big)^2 , \quad (36) \\ \alpha_3 - \alpha_1 = {} & 2v_{17}\lambda^2 \Big(\sum_{\mathbf{k},\omega_n} [G_\Gamma i\tau^y G_\Gamma]_{12}[G_X]_{11} \Big)^2 \\ & -2v_{13}\lambda^2 \Big(\sum_{\mathbf{k},\omega_n} [G_\Gamma]_{21}[G_X]_{12}[G_Y]_{12} \Big)^2 . \quad (37) \end{aligned}$$

Mapping these interactions back to the more familiar multi-orbital Hubbard model, as done in Ref. [39], reveals that $v_{13} = v_{15} = v_{17} = J$, while the non-contributing term is $v_{19} = U/2$. Thus, our microscopic calculation reveals that the low-energy magnetic anisotropy arises from a combination of the SOC and of the Hund's rule coupling. This anisotropy is present in the paramagnetic tetragonal phase, and does not require orbital or nematic order.

It is now straightforward to determine which of the three terms in the free energy Eq. (30) dominates. For instance, if both $\alpha_2 - \alpha_1 > 0$ and $\alpha_3 - \alpha_1 > 0$, α_1 is the smallest of the three coefficients and the ordered components of the magnetic moments will be $M_{1,x}$ and/or $M_{2,y}$. By evaluating the expressions in Eqs. (36) and (37) numerically, using the parameters that give the band dispersions and Fermi surface of Fig. 2, we can establish an effective "doping-temperature phase diagram" for the dominant anisotropy term as function of different values of the chemical potential μ and of the magnetic transition temperature T. Because the phase boundaries of this phase diagram are given by the conditions $\alpha_2 = \alpha_1$ or $\alpha_3 = \alpha_2$, and because these coefficients are independent of U and have J as an overall pre-factor (see Eqs. (36) and (37)), the phase boundaries do not change by varying U and J. The phase diagram, shown in fig. 6, reveals that for most of the parameter space considered here, the α_1 term is the smallest one, implying that the magnetic moments point parallel to their ordering vectors $\mathbf{Q}_i$ below the magnetic transition. There is a small range of parameters in which the moments lie in-plane, but perpendicular to their ordering vectors (i.e. α_2 is the smallest). Such a parameter regime is likely not relevant for the iron pnictides, since it would require an "undoped" composition (i.e. $\mu = 0$) to display a rather small magnetic transition temperature. Most interestingly, we find a robust region in which the moments point out-of-plane (i.e. α_3 is the smallest). This happens at any temperature, but always in the hole-doped side of the phase diagram ($\mu < 0$). In Fig. 7, we plot a zoom of the behavior of $\alpha_2 - \alpha_1$ and $\alpha_3 - \alpha_1$ as function of the chemical potential for two fixed temperatures to illustrate the different regimes obtained. Note that, for most of the phase diagram, $(\alpha_2 - \alpha_1) \ll (\alpha_3 - \alpha_1)$, regardless of the value of $J\lambda^2$, which appears as an overall prefactor of all α_i terms. This implies that the spin anisotropy behaves effectively as an easy-plane anisotropy. The fact that α_3 becomes the smallest coefficient in a narrow region of the phase diagram can be attributed to the fact that the term $\sum_{\mathbf{k},\omega_n} [G_\Gamma i\tau^y G_\Gamma]_{12}[G_X]_{11}$ in Eq. (37) changes sign from hole-doping to electron-doping. This behavior can be understood qualitatively by considering a hypotethical band structure in which all pockets are perfectly nested, $G_\Gamma = (i\omega_n + \varepsilon) \otimes \tau^0$ and $G_X = G_Y = (i\omega_n - \varepsilon) \otimes \tau^0$. A straightforward calculation reveals that the three-Green's function term above has different signs for $\mu > 0$ and $\mu < 0$, implying that it must vanish for a certain chemical potential value in the case of a realistic band structure.

Our results reveal not only an important asymmetry between electron- and hole-doping, but also agree qualitatively with experiments. In particular, neutron scattering measurements in hole- and electron-doped $\mathrm{BaFe_2As_2}$ [35–38] find generally in-plane moments parallel to $\mathbf{Q}_i$ in the magnetically-ordered state, except at a narrow hole-doping range in which the moments reorient and point out-of-the-plane.

IV. TETRAGONAL VS STRIPE MAGNETIC ORDER

The previous section established the direction of the magnetic moments, but not the magnetic ground state. For instance, from the analysis of the second-order terms of the free energy, it is impossible to distinguish the cases in which either $\mathbf{M}_1$ or $\mathbf{M}_2$ condense (i.e. $\mathbf{M}_2 = 0$ or $\mathbf{M}_1 = 0$) from the case in which both condense simultaneously ($\mathbf{M}_1 = \mathbf{M}_2 \neq 0$). The former case gives the striped orthorhombic magnetic phases shown in Fig. 3, whereas the latter case gives rise to a double-$\mathbf{Q}$ (i.e. biaxial) magnetic state that preserves the tetragonal symmetry of the system. From the form of the anisotropic terms in the free energy (see Sec. III), there are three

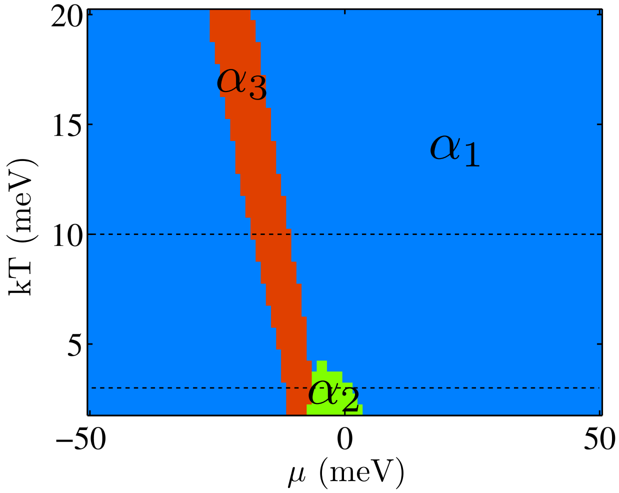

FIG. 6. Doping-temperature phase diagram displaying the smallest magnetic anisotropy coefficient α. When α_1 is the smallest, the moments point in-plane and parallel to the ordering vectors; when α_2 is the smallest, the moments point in-plane but perpendicular to the ordering vectors; finally, when α_3 is the smallest, the moments point out-of-plane. The corresponding uniaxial configurations are shown in Fig. 3. Note that temperature here actually refers to the magnetic transition temperature, as our model approaches the onset of long-range magnetic order from the paramagnetic state.

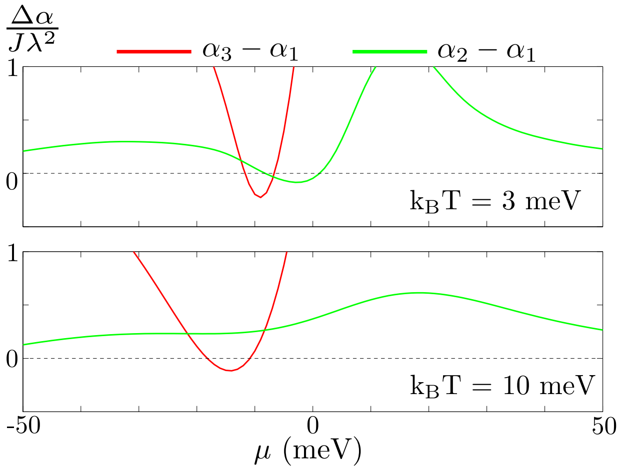

FIG. 7. Plots showing the dependence of $\alpha_3 - \alpha_1$ (red curve) and $\alpha_2 - \alpha_1$ (green curve) for two distinct temperatures (see the dashed lines in Fig. 6) as function of the chemical potential.

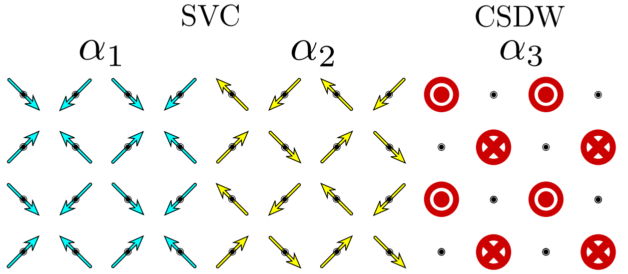

FIG. 8. Sketch of the three possible biaxial tetragonal magnetic phases. Here SVC is the spin vortex crystal phase (with non-collinear magnetic moments) and CSDW is the charge-spin density wave phase (with non-uniform magnetic moments).

different types of tetragonal magnetic ground states, as shown in Fig. 8. Two of them correspond to the so-called spin-vortex crystal phase (SVC), a non-collinear state in which $M_{1,x} = M_{2,y} \neq 0$ or $M_{1,y} = M_{2,x} \neq 0$, whereas the third one corresponds to the so-called charge-spin density-wave phase (CSDW) [51], a non-uniform state in which $M_{1,z} = M_{2,z} \neq 0$.

To determine whether the ground state corresponds to an orthorhombic uniaxial SDW (i.e. either $\mathbf{M}_1 \neq 0$ or $\mathbf{M}_2 \neq 0$) or to a tetragonal biaxial SDW (i.e. $\mathbf{M}_1 = \mathbf{M}_2 \neq 0$), we need to go to higher order in the free energy expansion. Symmetry requires the free energy to have the form (in the absence of SOC):

$$F^{(4)}(\mathbf{M}_1, \mathbf{M}_2) = \frac{u}{2}\left(\mathbf{M}_1^2 + \mathbf{M}_2^2\right)^2 - \frac{g}{2}\left(\mathbf{M}_1^2 - \mathbf{M}_2^2\right)^2 \quad (38)$$

$$+ 2w(\mathbf{M}_1 \cdot \mathbf{M}_2)^2 \,. \quad (39)$$

Minimizing this expression shows that the tetragonal biaxial state is realized when $g < 0$ or $g < -w$, whereas the orthorhombic uniaxial state takes place when $g > 0$ and $g > -w$.

The same model was derived by different itinerant approaches for the magnetic instabilities of the iron pnictides, revealing different parameter regimes in which the uniaxial or the biaxial states are the ground states [19, 21, 22, 48, 52–54]. In this regard, the novelty of our approach relies on the relationship between these ground states and the magnetic anisotropies, and also on the employment of a low-energy model that respects all symmetries of the FeAs plane, including the As puckering that enhances the size of the Fe unit cell. Because u and g are non-zero even for vanishing SOC and interactions, we compute only the contributions arising from the non-interacting part of the Hamiltonian. This is achieved either by standard diagrammatics or by explicitly integrating out the electronic degrees of freedom. We find:

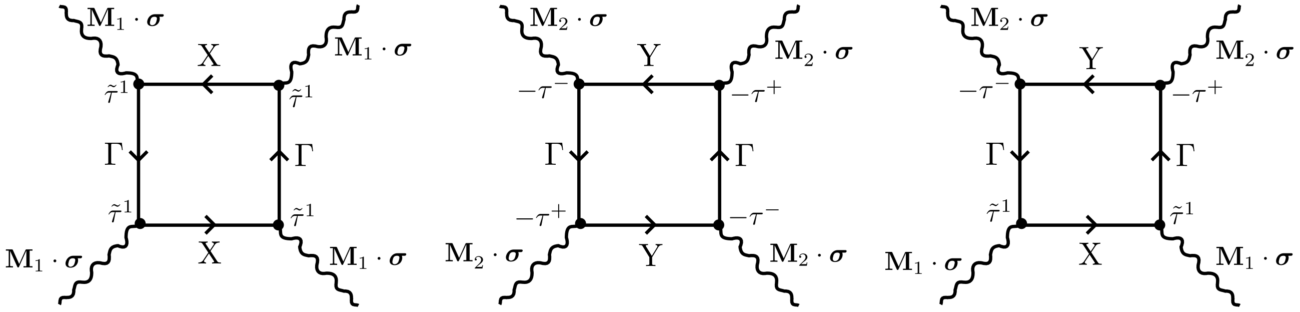

FIG. 9. Illustration of the three distinct fourth order diagrams that contribute to $F^{(4)}$. Note that the right diagram has a symmetry factor of two, while the symmetry factor of the middle and left diagrams is one. One might expect there to be a fourth diagram with alternating $\mathbf{M}_1$ and $\mathbf{M}_2$, however, the vertex coupling the SDW order parameter and the fermions forbids it (see Appendix D for more details).

$$\begin{aligned} F^{(4)} =& \mathbf{M}_1^4 \sum_{\mathbf{k},\omega_n} \mathrm{tr}\left(\tilde{\tau}^1 G_\Gamma \tilde{\tau}^1 G_X \tilde{\tau}^1 G_\Gamma \tilde{\tau}^1 G_X\right) \\ &+\mathbf{M}_2^4 \sum_{\mathbf{k},\omega_n} \mathrm{tr}\left(\tau^+ G_\Gamma \tau^- G_Y \tau^+ G_\Gamma \tau^- G_Y\right) \\ &+2\mathbf{M}_1^2\mathbf{M}_2^2 \sum_{\mathbf{k},\omega_n} \mathrm{tr}\left(\tau^+ G_\Gamma \tilde{\tau}^1 G_X \tilde{\tau}^1 G_\Gamma \tau^- G_Y\right) \\ F^{(4)} =& \mathbf{M}_1^4 \sum_{\mathbf{k},\omega_n} \left([G_\Gamma]_{11}^2 [G_X]_{11}^2\right) \\ &+\mathbf{M}_2^4 \sum_{\mathbf{k},\omega_n} \left([G_\Gamma]_{22}^2 [G_Y]_{11}^2\right) \\ &+2\mathbf{M}_1^2\mathbf{M}_2^2 \sum_{\mathbf{k},\omega_n} \left([G_\Gamma]_{12} [G_X]_{11} [G_Y]_{11}\right) , \end{aligned} \quad (40)$$

with the corresponding diagrams shown in Fig. 9. Rewriting the free energy in the form (38), we can readily obtain u, g, and w:

$$u = \sum_{\mathbf{k},\omega_n} \left([G_\Gamma]_{12}^2 [G_Y]_{11} [G_X]_{11} + [G_\Gamma]_{11}^2 [G_X]_{11}^2\right) \quad (41)$$

$$g = \sum_{\mathbf{k},\omega_n} \left([G_\Gamma]_{12}^2 [G_Y]_{11} [G_X]_{11} - [G_\Gamma]_{11}^2 [G_X]_{11}^2\right) \quad (42)$$

$$w = 0 \, . \quad (43)$$

One might expect the third diagram in Fig. 9 to result in a non-vanishing w, however, contraction of the Pauli matrices (see Eq. 31) reveals that the $\mathbf{M}_1 \cdot \mathbf{M}_2$ term cancels. More generally, $w = 0$ is a robust property of our model, a consequence of momentum conservation and the absence of a Fermi pocket at (π, π) (see Appendix D). Including a hole-pocket at (π, π) or interactions will however lead to a non-zero contribution to w [53].

We can now compute numerically the value of g for the same "doping-temperature phase-diagram" studied in the previous section, see Fig. 6. The combined result, shown in Fig. 10, accentuates the asymmetry between hole- and electron-doping discussed previously. In particular, while hole-doping tends to favor a tetragonal biaxial SDW state, electron-doping tends to favor an orthorhombic uniaxial SDW state. A cut with the behavior of g as function of μ for a fixed temperature is also shown in Fig. 11. To gain more insight into the behavior of g, we consider once again the hypothetical case of perfectly-nested bands, $G_\Gamma = (i\omega_n + \varepsilon) \otimes \tau^0$ and $G_X = G_Y = (i\omega_n - \varepsilon) \otimes \tau^0$. In this case, from the equations above, $g < 0$. Building on the results of Ref. [19], we expect that the sign of g will change once the two hole pockets become rather different in size, such that one of them becomes poorly nested with the electron pockets. Our calculations indicate that, for the general tight-binding model studied here, this is favored by hole doping rather than electron doping.

It is important to emphasize that these results should be understood as general trends as function of the chem-

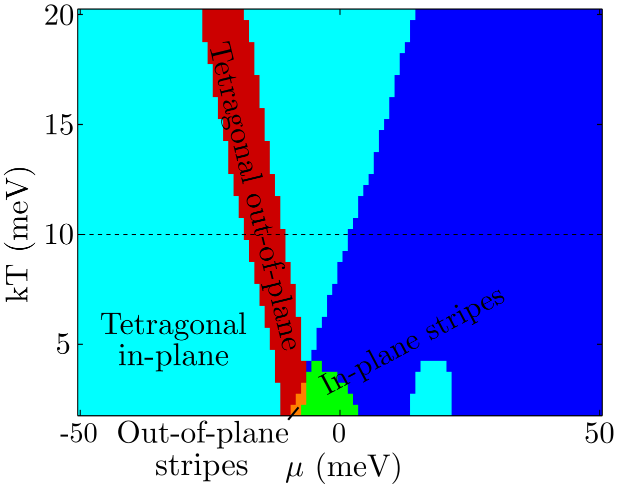

FIG. 10. Doping-temperature phase diagram of the different types of magnetic ground state (stripes or tetragonal) and their corresponding spin orientation (in-plane or out-of-plane). The color-code corresponds to the magnetic configurations shown in Figs. 3 and 8. Note that temperature here actually refers to the magnetic transition temperature, as our model approaches the onset of long-range magnetic order from the paramagnetic state.

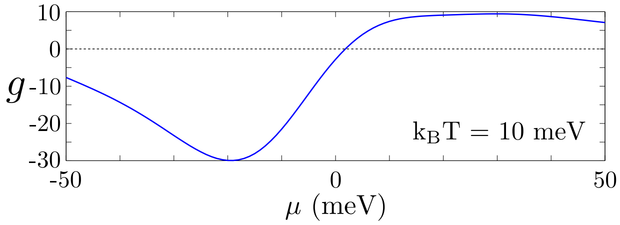

FIG. 11. The quartic coefficient g as a function of the chemical potential μ for a constant temperature (see the dashed line in Fig. 10). When g is negative the system chooses a tetragonal biaxial magnetic phase whereas for positive g, the system selects an orthorhombic uniaxial stripe state.

ical potential, rather than a full determination of the ground state for each specific value of μ. This is because, in contrast to the previous section, in which the lowest order contribution to the spin anisotropy arises solely from the SOC and the interactions, there are other potential contributions to g beyond the scope of the current work. Among these contributions, we highlight the sizable magneto-elastic coupling, which should extend the stripe phase to wider doping ranges [55, 56], and interaction corrections, which can also favor the uniaxial over the biaxial state [19, 53]. With this word of caution, we note that the tendency observed here that hole-doped compounds are more favorable to a tetragonal magnetic phase as compared to their electron-doped counterparts is in qualitative agreement with experiments, which observe a small region of tetragonal magnetism near the optimally-hole doped pnictides $\mathrm{Ba}_{1-x}\mathrm{Na}_x\mathrm{Fe}_2\mathrm{As}_2$ [57], $\mathrm{Sr}_{1-x}\mathrm{Na}_x\mathrm{Fe}_2\mathrm{As}_2$ [38], $\mathrm{Ba}_{1-x}\mathrm{K}_x\mathrm{Fe}_2\mathrm{As}_2$ [58, 59], and $\mathrm{Ba}(\mathrm{Fe}_{1-x}\mathrm{Mn}_x)_2\mathrm{As}_2$ [60].

Interestingly, in the first three compounds, neutron scattering has shown that the onset of a tetragonal magnetic state takes place in a region in which the magnetic moments reorient from in-plane to out-of-plane. Within our analysis, this can be attributed to the robust region in parameter space in which α_3 is the smallest anisotropic coefficient (see Fig. 10). More importantly, this anisotropic coefficient removes the degeneracy between the two types of tetragonal SDW phase – the SVC and the CSDW states (see Fig. 8) – by favoring the latter. This is expected to happen even if $w \neq 0$, since the latter is a quartic coefficient, whereas α_3 is a quadratic coefficient. Therefore, at least near the onset of the magnetic transition, it is the SOC and the Hund's rule coupling that select the CSDW phase. Recently, Mössbauer [38] and μSR [61] experiments in $\mathrm{Sr}_{1-x}\mathrm{Na}_x\mathrm{Fe}_2\mathrm{As}_2$ and $\mathrm{Ba}_{1-x}\mathrm{K}_x\mathrm{Fe}_2\mathrm{As}_2$, respectively, have reported direct evidence that indeed the CSDW state is realized in the regime where the spin is reoriented and the magnetic long-range order preserves tetragonal symmetry.

V. DISCUSSION AND CONCLUSIONS

In summary, we have shown that within a low-energy model that respects the symmetries of the FeAs plane, magnetic anisotropy arises naturally from the combination of the spin-orbit coupling and the Hund's rule coupling. The magnetic anisotropy consists of three terms (see Sec. III). Although it cannot be mapped generally on an easy-axis or an easy-plane term, it effectively behaves as an easy-plane term for a large part of the parameter region studied here, since $(\alpha_2 - \alpha_1) \ll (\alpha_3 - \alpha_1)$. We found that, for most of the temperature-doping phase diagram, the spin anisotropy is such that the magnetic moments point in-plane and parallel to the direction of the ordering vector. For a small doping range in the hole-doped side, across all temperatures studied, the magnetic moments tend to reorient and point out-of-plane. These features are consistent with those observed experimentally, including the spin reorientation observed in the hole-doped pnictides $\mathrm{Ba}_{1-x}\mathrm{Na}_x\mathrm{Fe}_2\mathrm{As}_2$ [35], $\mathrm{Sr}_{1-x}\mathrm{Na}_x\mathrm{Fe}_2\mathrm{As}_2$ [38], $\mathrm{Ba}_{1-x}\mathrm{K}_x\mathrm{Fe}_2\mathrm{As}_2$ [37]. We also found a general tendency of tetragonal double-$\mathbf{Q}$ magnetic order for the hole-doped side of the phase diagram, whereas the orthorhombic single-$\mathbf{Q}$ stripe magnetic order is favored in the electron-doped side. Although this is in general agreement with the experimental observations in $\mathrm{Ba}_{1-x}\mathrm{Na}_x\mathrm{Fe}_2\mathrm{As}_2$ [57], $\mathrm{Sr}_{1-x}\mathrm{Na}_x\mathrm{Fe}_2\mathrm{As}_2$ [38], $\mathrm{Ba}_{1-x}\mathrm{K}_x\mathrm{Fe}_2\mathrm{As}_2$ [58], and $\mathrm{Ba}(\mathrm{Fe}_{1-x}\mathrm{Mn}_x)_2\mathrm{As}_2$ [60], our results seem to overestimate the size of the region in which the tetragonal magnetic state is stable. A possible reason for this discrepancy is that our model does not account for other factors that usually favor the stripe over the tetragonal magnetic state, such as the magneto-elastic coupling [55, 56] and the residual interactions not directly responsible for the SDW instability [19, 53]. Yet, our results provide a clear connection between the spin reorientation and the type of tetragonal magnetic state observed in the hole-doped iron pnictides – namely, the charge-spin density-wave state with a non-uniform magnetization [38, 61].

An important consequence of our results is that the spin anisotropy is not necessarily tied to the orbital order that is triggered across the nematic/structural transition [30]. Although it is plausible that such an orbital order affects the spin anisotropy, the latter exists already in the tetragonal paramagnetic state as a result of the symmetry properties of the FeAs plane. In this regard, it would be interesting to investigate how the spin anisotropies in the tetragonal-paramagnetic phase studied here are connected to the spin anisotropies in the low-temperature phase, after both magnetic and nematic orders are well established. Finally, our results open the important question of how this particular form of magnetic anisotropy impacts the normal state properties of the iron pnictides. In particular, the onset temperatures and the characters of the coupled nematic-magnetic transitions are expected to be strongly affected by any form of spin anisotropy [14, 30, 62].

ACKNOWLEDGEMENTS

We thank F. Ahn, M. Schulz, A. Chubukov, P. Dai, P. Orth, J. Knolle, M. Korshunov, R. Osborn, P. Hirschfeld, Y. Zhao and O. Vafek for fruitful discussions. MHC and BMA acknowledge financial support from a Lundbeckfond fellowship (grant A9318). RMF and JK are supported by the U.S. Department of Energy, Office of Science, Basic Energy Sciences, under award number DE-SC0012336. The work of IE was supported by the Focus Program 1458 Eisen-Pniktide of the DFG, and by the German Academic Exchange Service (DAAD PPP USA no. 57051534). IE also acknowledges the financial support of the Ministry of Education and Science of the Russian Federation in the framework of Increase Competitiveness Program of NUST MISiS (N 2-2014-015).

---

[1] A. V. Chubukov, Ann. Rev. Cond. Mat. Phys. **3** 57 (2012).
[2] P. J. Hirschfeld, M. M. Korshunov and I. I. Mazin, Rep. Prog. Phys. **74** 124508 (2011).
[3] K. Ishida, Y. Nakai and H. Hosono, J. Phys. Soc. Jpn. **78**, 062001 (2009).
[4] J. Paglione and R. L. Greene, Nat. Phys. **6**, 645 (2010).
[5] D. S. Inosov, Comptes Rendus Physique (2015), DOI:10.1016/j.crhy.2015.03.001.
[6] P. Dai, arXiv:1503:02340.
[7] I. I. Mazin and M. D. Johannes, Nat. Phys. **5**, 141 (2009).
[8] P. Dai, J. Hu and E. Dagotto, Nat. Phys. **8**, 709 (2012).
[9] C. Fang, H. Yao, W. Tsai, J. Hu and S. A. Kivelson, Phys. Rev. B **77**, 224509 (2008).
[10] F. Krüger, S. Kumar, J. Zaanen and J. van den Brink, Phys. Rev. B **79**, 054504 (2009).
[11] C. Xu, M. Müller and S. Sachdev, Phys. Rev. B **78**, 020501(R) (2008).
[12] E. Abrahams and Q. Si, J. Phys. Condens. Matter **23**, 223201 (2011).
[13] Y. Kamiya, N. Kawashima and C. D. Batista, Phys. Rev. B **84**, 214429 (2011).
[14] R. M. Fernandes, A. V. Chubukov, J. Knolle, I. Eremin and J. Schmalian, Phys. Rev. B **85**, 024534 (2012).
[15] A.V. Chubukov, D. Efremov, and I. Eremin, Phys. Rev. B **78**, 134512 (2008).
[16] H.-H. Klauss, H. Luetkens, R. Klingeler, C. Hess, F.J. Litterst, M. Kraken, M. M. Korshunov, I. Eremin, S.-L. Drechsler, R. Khasanov, A. Amato, J. Hamann-Borreo, N. Leps, A. Kondrat, G. Behr, J. Werner, B. Büchner, Phys. Rev. Lett. **101**, 077005 (2008); M. M. Korshunov, and I. Eremin, Europhys. Lett. **83**, 67003 (2008).
[17] J. Knolle, I. Eremin, A. V. Chubukov, and R. Moessner, Phys. Rev. B **81**, 140506(R) (2010).
[18] M. Kovacic, M. H. Christensen, M. N. Gastiasoro, B. M. Andersen, Phys. Rev. B **91**, 064424 (2015).
[19] I. Eremin and A. V. Chubukov, Phys. Rev. B **81**, 024511 (2011).
[20] V. Cvetkovic and Z. Tesanovic, Phys. Rev. B **80**, 024512 (2009).
[21] P. M. R. Brydon and C. Timm, Phys. Rev. B **79**, 180504(R) (2009).
[22] J. Lorenzana, G. Seibold, C. Ortix and M. Grilli, Phys. Rev. Lett. **101**, 186402 (2008).
[23] S. Liang, A. Moreo, and E. Dagotto, Phys. Rev. Lett. **111**, 047004 (2013).
[24] S. Ducatman, R. M. Fernandes and N. B. Perkins, Phys. Rev. B **90** 165123 (2014).
[25] W. Yin, C. Lee and W. Ku, Phys. Rev. Lett. **105** 107004 (2010).
[26] W. Lv, F. Krüger and P. Phillips, Phys. Rev. B **82** 045125 (2010).
[27] M. D. Johannes and I. I. Mazin, Phys. Rev. B **79**, 220510 (2009).
[28] L. Fanfarillo, A. Cortijo and B. Valenzuela, Phys. Rev. B **91**, 214515 (2015).
[29] R. M. Fernandes, A. V. Chubukov and J. Schmalian, Nat. Phys. **10**, 97 (2014).
[30] R. Applegate, R. R. P. Singh, C. Chen and T. P. Devereaux, Phys. Rev. B **85**, 054411 (2012).
[31] G. S. Tucker, R. M. Fernandes, D. K. Pratt, A. Thaler, N. Ni, K. Marty, A. D. Christianson, M. D. Lumsden, B. C. Sales, A. S. Sefat, S. L. Bud'ko, P. C. Canfield, A. Kreyssig, A. I. Goldman, and R. J. McQueeney, Phys. Rev. B **89** 180503(R) (2014).
[32] J. T. Park, G. Friemel, T. Loew, V. Hinkov, Yuan Li, B. H. Min, D. L. Sun, A. Ivanov, A. Piovano, C. T. Lin, B. Keimer, Y. S. Kwon, and D. S. Inosov, Phys. Rev. B **86**, 024437 (2012).
[33] Y. Song, L. Regnault, C. Zhang, G. Tan, S. V. Carr, S. Chi, A. D. Christianson, T. Xiang, and P. Dai, Phys. Rev. B **88**, 134512 (2013).
[34] H. Luo, M. Wang, C. Zhang, X. Lu, L. Regnault, R. Zhang, S. Li, J. Hu, and P. Dai, Phys. Rev. Lett. **111**, 107006 (2013).
[35] F. Waßer, A. Schneidewind, Y. Sidis, S. Wurmehl, S. Aswartham. B. Büchner, and M. Braden, Phys. Rev. B **91** 060505(R) (2015).
[36] D. D. Khalyavin, S. W. Lovesey, P. Manuel, F. Krüger, S. Rosenkranz, J. M. Allred, O. Chmaissem and R. Osborn, Phys. Rev. B **90**, 174511 (2014).
[37] J. M. Allred, S. Avci, D. Y. Chung, H. Claus, D. D. Khalyavin, P. Manuel, K. M. Taddei, M. G. Kanatzadis, S. Rosenkranz, R. Osborn, and O. Chmaissem, Phys. Rev. B **92**, 094515 (2015).
[38] J. M. Allred, K. M. Taddei, D. E. Bugaris, M. J. Krogstad, S. H. Lapidus, D. Y. Chung, H. Claus, M. G. Kanatzidis, D. E. Brown, J. Kang, R. M. Fernandes, I. Eremin, S. Rosenkranz, O. Chmaissem, and R. Osborn, arXiv:1505.06175.
[39] V. Cvetkovic and O. Vafek, Phys. Rev. B **88**, 134510 (2013).
[40] R. M. Fernandes and O. Vafek, Phys. Rev. B **90**, 214514 (2014).
[41] M. M. Korshunov, Y. N. Togushova. I. Eremin and P. J. Hirschfeld, J. Supercond. Novel Magn. **26**, 2873 (2013).
[42] E. M. Nica, R. Yu and Q. Si, arXiv:1505.04227.
[43] S. Borisenko, D. Evtushinsky, I. Morozov, S. Wurmehl, B. Büchner, A. Yaresko, T. Kim and M. Hoesch, arXiv:1409.8669

[44] M. Nakajima, S. Ishida, K. Kihou, Y. Tomioka, T. Ito, Y. Yoshida, C. H. Lee, H. Kito, A. Iyo, H. Eisaki, K. M. Kojima, and S. Uchida, Phys. Rev. B **81**, 104528 (2010).

[45] A. Lucarelli, A. Dusza, F. Pfuner, P. Lerch, J. G. Analytis, J.-H Chu, I. R. Fisher, and L. Degiorgi, New J. Phys. **12**, 073036 (2010).

[46] S. Graser, T. A. Maier, P. J. Hirschfeld and D. J. Scalapino, New J. Phys. **11**, 025016 (2009)

[47] V. Cvetkovic and Z. Tesanovic, Europhys. Lett. **85**, 37002 (2009)

[48] M. N. Gastiasoro and B. M. Andersen, Phys. Rev. B **92**, 140506(R) (2015).

[49] M. Daghofer, A. Nicholson, A. Moreo and E. Dagotto, Phys. Rev. B **81** 014511 (2010).

[50] F. Ahn, private communication.

[51] R. M. Fernandes, S. A. Kivelson and E. Berg, arXiv:1504.03656.

[52] J. Kang, X. Wang, A.V. Chubukov and R. M. Fernandes, Phys. Rev. B **91**, 121104(R) (2015).

[53] X. Wang, J. Kang and R. M. Fernandes, Phys. Rev. B **91**, 024401 (2015).

[54] G. Giovannetti, C. Ortix, M. Marsman, M. Capone, J. van den Brink and J. Lorenzana, Nat. Commun. **2**, 398 (2011).

[55] R. M. Fernandes, L. H. VanBebber, S. Bhattacharya, P. Chandra, V. Keppens, D. Mandrus, M. A. McGuire, B. C. Sales, A. S. Sefat, and J. Schmalian, Phys. Rev. Lett. **105**, 157003 (2010).

[56] I. Paul, Phys. Rev. Lett. **107**, 047004 (2011).

[57] S. Avci, O. Chmaissem, J. M. Allred, S. Rosenkranz, I. Eremin, A. V. Chubukov, D. E. Bugaris, D. Y. Chung, M. G. Kanatzidis, J.-P Castellan, J. A. Schlueter, H. Claus, D. D. Khalyavin, P. Manuel, A. Daoud-Aladine, and R. Osborn, Nat. Commun. **5**, 3845 (2014).

[58] A. E. Böhmer, F. Hardy, L. Wang, T. Wolf, P. Schweiss, and C. Meingast, Nat. Commun. **6**, 7911 (2015).

[59] B. P. P. Mallett, P. Marsik, M. Yazdi-Rizi, Th. Wolf, A. E. Böhmer, F. Hardy, C. Meingast, D. Munzar and C. Bernhard, Phys. Rev. Lett. **115**, 027003 (2015)

[60] M. G. Kim, A. Kreyssig, A. Thaler, D. K. Pratt, W. Tian, J. L. Zarestky, M. A. Green, S. L. Bud'ko, P. C. Canfield, R. J. McQueeney, and A. I. Goldman, Phys. Rev. B **82**, 220503(R) (2010).

[61] B. P. P. Mallett, Y. G. Pashkevich, A. Gusev, T. Wolf and C. Bernhard, arXiv:1506.00786.

[62] M. Capati, M. Grilli, and J. Lorenzana Phys. Rev. B **84**, 214520 (2011).

[63] K. K. Ng and M. Sigrist, Europhys. Lett. **49**, 473 (2000).

Appendix A: Expansion of tight-binding Hamiltonian for small k

In this appendix we derive explicitly the non-interacting Hamiltonian H_0 introduced in sec. II. As explained in that section, we need to project and expand the 5-orbital tight-binding dispersion $\varepsilon_{\mu\nu}(\mathbf{k})$, where $\mu, \nu = 1, ..., 5$ are the orbital indices corresponding to xz, yz, x^2-y^2, xy and $3z^2-r^2$, respectively. The dispersions are given by [46]

$$\begin{aligned}
\varepsilon_{11} &= \epsilon_{xz/yz} + 2t^{11}_{x}\cos k_x + 2t^{11}_{y}\cos k_y + 4t^{11}_{xy}\cos k_x\cos k_y + 2t^{11}_{xx/yy}\left(\cos 2k_x - \cos 2k_y\right) \\
&\quad + 4t^{11}_{xxy}\cos 2k_x\cos k_y + 4t^{11}_{xyy}\cos k_x\cos 2k_y + 4t^{11}_{xxyy}\cos 2k_x\cos 2k_y\,, && \text{(A1)} \\
\varepsilon_{22} &= \epsilon_{xz/yz} + 2t^{22}_{x}\cos k_x + 2t^{22}_{y}\cos k_y + 4t^{22}_{xy}\cos k_x\cos k_y - 2t^{22}_{xx/yy}\left(\cos 2k_x - \cos 2k_y\right) \\
&\quad + 4t^{22}_{xxy}\cos 2k_x\cos k_y + 4t^{22}_{xyy}\cos k_x\cos 2k_y + 4t^{22}_{xxyy}\cos 2k_x\cos 2k_y\,, && \text{(A2)} \\
\varepsilon_{33} &= \epsilon_{x^2-y^2} + 2t^{33}_{x/y}\left(\cos k_x + \cos k_y\right) + 4t^{33}_{xy}\cos k_x\cos k_y 2t^{33}_{xx/yy}\left(\cos 2k_x + \cos 2k_y\right)\,, && \text{(A3)} \\
\varepsilon_{44} &= \epsilon_{xy} + 2t^{44}_{x/y}\left(\cos k_x + \cos k_y\right) + t^{44}_{xy}\cos k_x\cos k_y + 2t^{44}_{xx/yy}\left(\cos 2k_x + \cos 2k_y\right) \\
&\quad + 4t^{44}_{xxy/xyy}\left(\cos 2k_x\cos k_y + \cos k_x\cos 2k_y\right) + 4t^{44}_{xxyy}\cos 2k_x\cos 2k_y\,, && \text{(A4)} \\
\varepsilon_{55} &= \epsilon_{z^2} + 2t^{55}_{x/y}\left(\cos k_x + \cos k_y\right) + 2t^{55}_{xx/yy}\left(\cos 2k_x\cos 2k_y\right) \\
&\quad + 4t^{55}_{xxy/xyy}\left(\cos 2k_x\cos k_y + \cos k_x\cos 2k_y\right) + 4t^{55}_{xxyy}\cos 2k_x\cos 2k_y\,, && \text{(A5)} \\
\varepsilon_{12} &= 4t^{12}_{xy}\sin k_x\sin k_y + 4t^{12}_{xxy/xyy}\left(\sin 2k_x\sin k_y + \sin k_x\sin 2k_y\right) + 4t^{12}_{xxyy}\sin 2k_x\sin 2k_y\,, && \text{(A6)} \\
\varepsilon_{13} &= i2t^{13}_{y}\sin k_y + i4t^{13}_{xy}\cos k_x\sin k_y - i4t^{13}_{xxy/xyy}\left(\cos k_x\sin 2k_y - \cos 2k_x\sin k_y\right)\,, && \text{(A7)} \\
\varepsilon_{14} &= i2t^{14}_{x}\sin k_x - i4t^{14}_{xy}\sin k_x\cos k_y + i4t^{14}_{xxy}\sin 2k_x\cos k_y\,, && \text{(A8)} \\
\varepsilon_{15} &= i2t^{15}_{y}\sin k_y - i4t^{15}_{xy}\cos k_x\sin k_y - i4t^{15}_{xxyy}\cos 2k_x\sin 2k_y\,, && \text{(A9)} \\
\varepsilon_{23} &= i2t^{23}_{x}\sin k_x + i4t^{23}_{xy}\sin k_x\cos k_y - i4t^{23}_{xxy/xyy}\left(\sin 2k_x\cos k_y - \sin k_x\cos 2k_y\right)\,, && \text{(A10)} \\
\varepsilon_{24} &= -i2t^{24}_{y}\sin k_y + i4t^{24}_{xy}\cos k_x\sin k_y - i4t^{24}_{xyy}\cos k_x\sin 2k_y\,, && \text{(A11)} \\
\varepsilon_{25} &= -i2t^{25}_{x}\sin k_x + i4t^{25}_{xy}\sin k_x\cos k_y + i4t^{25}_{xxyy}\sin 2k_x\cos 2k_y\,, && \text{(A12)} \\
\varepsilon_{34} &= 4t^{34}_{xxy/xyy}\left(\sin k_x\sin 2k_y - \sin 2k_x\sin k_y\right)\,, && \text{(A13)} \\
\varepsilon_{35} &= 2t^{35}_{x/y}\left(\cos k_x - \cos k_y\right) + 4t^{35}_{xxy/xyy}\left(\cos 2k_x\cos k_y - \cos k_x\cos 2k_y\right)\,, && \text{(A14)} \\
\varepsilon_{45} &= 4t^{45}_{xy}\sin k_x\sin k_y + 4t^{45}_{xxyy}\sin 2k_x\sin 2k_y\,. && \text{(A15)}
\end{aligned}$$

Here ϵ_i are the onsite energies associated with each orbital and $t^{\mu\nu}_{ij}$ are hopping parameters from orbital μ on site i to orbital ν on site j. The above expressions are accompanied by constraints on the coefficients $t^{\mu\nu}_{ij}$ due to tetragonal symmetry:

$$\begin{array}{cccc} t^{11}_{x} = t^{22}_{y} & t^{11}_{y} = t^{22}_{x} & t^{11}_{xy} = t^{22}_{xy} & t^{11}_{xx/yy} = t^{22,xx/yy} \\ t^{11}_{xxy} = t^{22}_{xyy} & t^{11}_{xyy} = t^{22}_{xxy} & t^{11}_{xxyy} = t^{22}_{xxyy} & t^{13}_{y} = t^{23}_{x} \\ t^{13}_{xy} = t^{23}_{xy} & t^{13}_{xxy/xyy} = t^{23}_{xxy/xyy} & t^{14}_{x} = t^{24}_{y} & t^{14}_{xy} = t^{24}_{xy} \\ t^{14}_{xxy} = t^{24}_{xyy} & t^{15}_{y} = t^{25}_{x} & t^{15}_{xy} = t^{25}_{xy} & t^{15}_{xxyy} = t^{25}_{xxyy} \,. \end{array} \tag{A16}$$

We are now in a position to expand the elements of $\varepsilon_{\mu\nu}(\mathbf{k})$ around the Γ, X and Y points. At the Γ point the orbitals xz and yz dominate, corresponding to the elements ε_{11}, ε_{12}, ε_{21} and ε_{22}. Similarly, at the X (Y) point the dominant orbitals are yz (xz) and xy. To obtain these parts we expand ε_{22} (ε_{11}), ε_{24} (ε_{14}) and ε_{44} around $(k_x+\pi, k_y)$ ($(k_x, k_y+\pi)$):

$$h_\Gamma = \begin{pmatrix} C_1 + C_2\left(k_x^2+k_y^2\right) + C_3\left(k_x^2-k_y^2\right) & C_4 k_x k_y \\ C_4 k_x k_y & C_1 + C_2\left(k_x^2+k_y^2\right) - C_3\left(k_x^2-k_y^2\right) \end{pmatrix} \tag{A17}$$

$$h_X = \begin{pmatrix} C_5 + C_6\left(k_x^2+k_y^2\right) + C_7\left(k_x^2-k_y^2\right) & -iv_X(\mathbf{k}) \\ iv_X(\mathbf{k}) & C_{11} + C_{12}\left(k_x^2+k_y^2\right) + C_{13}\left(k_x^2-k_y^2\right) \end{pmatrix} \tag{A18}$$

$$h_Y = \begin{pmatrix} C_5 + C_6\left(k_x^2+k_y^2\right) - C_7\left(k_x^2-k_y^2\right) & -iv_Y(\mathbf{k}) \\ iv_Y(\mathbf{k}) & C_{11} + C_{12}\left(k_x^2+k_y^2\right) - C_{13}\left(k_x^2-k_y^2\right) \end{pmatrix}, \tag{A19}$$

where

$$v_X(\mathbf{k}) = C_8 k_y + C_9 k_y\left(k_y^2+3k_x^2\right) - C_{10} k_y\left(k_x^2-k_y^2\right) \tag{A20}$$

$$v_Y(\mathbf{k}) = -C_8 k_x - C_9 k_x\left(k_x^2+3k_y^2\right) - C_{10} k_x\left(k_x^2-k_y^2\right) \tag{A21}$$

As a function of the tight-binding parameters, the constants $C_1, \ldots, C_{13}$ are

$$C_1 = \epsilon_\Gamma = \epsilon_{xz/yz} + 2\left(t^{11}_x + t^{11}_y\right) + 4\left(t^{11}_{xxy} + t^{11}_{xyy} + t^{11}_{xy} + t^{11}_{xxyy}\right) \tag{A22}$$

$$C_2 = 2\frac{1}{2m_\Gamma} = -\frac{1}{2}\left(t^{11}_x + t^{11}_y\right) - 5\left(t^{11}_{xxy} + t^{11}_{xyy}\right) - 2t^{11}_{xy} - 8t^{11}_{xxyy} \tag{A23}$$

$$C_3 = b = \frac{1}{2}\left(t^{11}_y - t^{11}_x\right) + 3\left(t^{11}_{xyy} - t^{11}_{xxy}\right) - 4t^{11}_{xx/yy} \tag{A24}$$

$$C_4 = 4c = -4\left(t^{12}_{xy} + 4t^{12}_{xxyy} + 4t^{12}_{xxy/xyy}\right) \tag{A25}$$

$$C_5 = \epsilon_1 = \epsilon_{xz/yz} + 2\left(t^{11}_x - t^{11}_y\right) - 4\left(t^{11}_{xxy} - t^{11}_{xyy} + 4t^{11}_{xy} - 4t^{11}_{xxyy}\right) \tag{A26}$$

$$C_6 = 2\frac{1}{2m_1} = \frac{1}{2}\left(t^{11}_y - t^{11}_x\right) + 5\left(t^{11}_{xxy} - t^{11}_{xyy}\right) + 2t^{11}_{xy} - 8t^{11}_{xxyy} \tag{A27}$$

$$C_7 = a_1 = \frac{1}{2}\left(t^{11}_x + t^{11}_y\right) - 3\left(t^{11}_{xxy} + t^{11}_{xyy}\right) + 4t^{11}_{xx/yy} \tag{A28}$$

$$C_8 = 2v = 2\left(t^{14}_y + 2t^{14}_{xy} - 4t^{14}_{xxy}\right) \tag{A29}$$

$$C_9 = 2p_1 = -\frac{1}{12}t^{24}_y - \frac{25}{6}t^{24}_{xy} + \frac{7}{3}t^{24}_{xyy} \tag{A30}$$

$$C_{10} = 2p_2 = -\frac{1}{4}t^{24}_y + 3t^{24}_{xyy} \tag{A31}$$

$$C_{11} = \epsilon_3 = \epsilon_{xy} + 4\left(-t^{44}_{xy} + t^{44}_{xx/yy} + t^{44}_{xxyy}\right) \tag{A32}$$

$$C_{12} = 2\frac{1}{2m_3} = 2\left(t^{44}_{xy} - 2t^{44}_{xx/yy} - 4t^{44}_{xxyy}\right) \tag{A33}$$

$$C_{13} = a_3 = t^{44}_{x/y} - 6t^{44}_{xxy/xyy}\,. \tag{A34}$$

The overall minus sign in the coefficient C_4 arises due to the minus sign in the definition of the spinor in Eq. (4). The coefficients can be obtained either by using the relations above with the coefficients $t^{\mu\nu}_{ij}$ determined from tight-binding fits to DFT calculations, or by directly fitting the coefficients to DFT calculations.

Appendix B: Spin-orbit coupling in orbital basis

Here we express the standard spin-orbit coupling term $\lambda\mathbf{S}\cdot\mathbf{L}$ in the orbital basis, which leads to Eqs. (19)-(21) of the main text. Denote the eigenstates of L_z by $|m\rangle$

where $m = -L, \dots, L$. The spin-orbit Hamiltonian is then

$$H_{\mathrm{SOC}} = \sum_{\substack{mn\\ \alpha\beta}} \langle m\alpha | \lambda \mathbf{S} \cdot \mathbf{L} | n\beta \rangle d^\dagger_{m\alpha} d_{n\beta} \,. \tag{B1}$$

where $d^\dagger_{m\alpha}$ creates an electron with spin α and angular momentum projection m. Using the fact that $\mathbf{S}\cdot\mathbf{L} = L_z S_z + \frac{1}{2}(L^+ S^- + L^- S^+)$ and

$$S_z |n\alpha\rangle = \pm \frac{1}{2} |n\alpha\rangle \,, \quad S^\pm |n\alpha\rangle = \delta_{\alpha, \mp\frac{1}{2}} |n, \alpha \pm 1\rangle \,, \tag{B2}$$

the Hamiltonian becomes

$$\begin{aligned} H_{\mathrm{SOC}} &= \frac{\lambda}{2} \sum_{mn} \Big[\langle m|L_z|n\rangle d^\dagger_{m\uparrow} d_{n\uparrow} - \langle m|L_z|n\rangle d^\dagger_{m\downarrow} d_{n\downarrow} \\ &\quad + \langle m|L^+|n\rangle d^\dagger_{m\downarrow} d_{n\uparrow} + \langle m|L^-|n\rangle d^\dagger_{m\uparrow} d_{n\downarrow} \Big] \\ &= \frac{\lambda}{2} \sum_{\substack{mn\\ \alpha\beta}} A^{\alpha\beta}_{mn} d^\dagger_{m\alpha} d_{n\beta} \,, \end{aligned} \tag{B3}$$

with the matrix elements:

$$A^{\uparrow\uparrow}_{mn} = -A^{\downarrow\downarrow}_{mn} = \langle m|L_z|n\rangle = n\delta_{mn} \tag{B4}$$

$$A^{\downarrow\uparrow}_{mn} = \sqrt{(L-n)(L+n+1)}\delta_{m,n+1} \tag{B5}$$

$$A^{\uparrow\downarrow}_{mn} = \sqrt{(L+n)(L-n+1)}\delta_{m,n-1} \,. \tag{B6}$$

We can transform the Hamiltonian in Eq. B3 to the basis spanned by the cubic harmonics (i.e. the orbital basis) using

$$d_{m\alpha} = \sum_\mu U_{m\mu} c_{\mu\alpha} \tag{B7}$$

$$d^\dagger_{m\alpha} = \sum_\mu U^*_{m\mu} c^\dagger_{\mu\alpha} \,, \tag{B8}$$

where $U_{m\mu} \equiv \langle m|\mu\rangle$ and $|\mu\rangle$ is the basis states in the space of cubic harmonics. The transformed Hamiltonian is

$$H_{\mathrm{SOC}} = \frac{\lambda}{2} \sum_{\substack{\mu\nu\\ \alpha\beta}} \widetilde{A}^{\alpha\beta}_{\mu\nu} c^\dagger_{\mu\alpha} c_{\nu\beta} \,, \tag{B9}$$

with $\widetilde{A}^{\alpha\beta} = U^\dagger A^{\alpha\beta} U$.

To proceed we specialize to the case $L = 2$, resulting in the well-known d-orbitals. The basis states are $\langle\mu| = \langle xz|, \langle yz|, \langle xy|, \langle x^2-y^2|, \langle z^2|$ with

$$\langle xz| = \frac{1}{\sqrt{2}} \left(-\langle 1| + \langle -1| \right) \tag{B10}$$

$$\langle yz| = \frac{i}{\sqrt{2}} \left(-\langle 1| - \langle -1| \right) \tag{B11}$$

$$\langle xy| = \frac{i}{\sqrt{2}} \left(-\langle -2| + \langle 2| \right) \tag{B12}$$

$$\langle x^2-y^2| = \frac{1}{\sqrt{2}} \left(\langle -2| + \langle 2| \right) \tag{B13}$$

$$\langle z^2| = \langle 0| \,, \tag{B14}$$

and $U^\dagger$ can be read off as the coefficients of these equations. Thus, we find U to be

$$U = \frac{1}{\sqrt{2}} \begin{pmatrix} 0 & 0 & -i & 1 & 0 \\ -1 & i & 0 & 0 & 0 \\ 0 & 0 & 0 & 0 & \sqrt{2} \\ 1 & i & 0 & 0 & 0 \\ 0 & 0 & i & 1 & 0 \end{pmatrix} \,, \tag{B15}$$

yielding the three independent $\widetilde{A}$-matrices:

$$\widetilde{A}^{\uparrow\uparrow} = \begin{pmatrix} 0 & -i & 0 & 0 & 0 \\ i & 0 & 0 & 0 & 0 \\ 0 & 0 & 0 & i2 & 0 \\ 0 & 0 & -i2 & 0 & 0 \\ 0 & 0 & 0 & 0 & 0 \end{pmatrix} \,, \tag{B16}$$

$$\widetilde{A}^{\downarrow\uparrow} = \begin{pmatrix} 0 & 0 & i & 1 & -\sqrt{3} \\ 0 & 0 & 1 & -i & -i\sqrt{3} \\ -i & -1 & 0 & 0 & 0 \\ -1 & i & 0 & 0 & 0 \\ \sqrt{3} & i\sqrt{3} & 0 & 0 & 0 \end{pmatrix} \,, \tag{B17}$$

$$\widetilde{A}^{\uparrow\downarrow} = \begin{pmatrix} 0 & 0 & i & -1 & \sqrt{3} \\ 0 & 0 & -1 & -i & -i\sqrt{3} \\ -i & 1 & 0 & 0 & 0 \\ 1 & i & 0 & 0 & 0 \\ -\sqrt{3} & i\sqrt{3} & 0 & 0 & 0 \end{pmatrix} \,. \tag{B18}$$

$$\tag{B19}$$

Considering only the $|xz\rangle$, $|yz\rangle$ and $|xy\rangle$ orbitals, corresponding to the upper left 3×3 blocks in the above matrices results in the restricted matrix $\widetilde{A'}^{\alpha\beta}_{\mu'\nu'}$:

$$\widetilde{A'} = \begin{pmatrix} 0 & -i & 0 & 0 & 0 & i \\ i & 0 & 0 & 0 & 0 & -1 \\ 0 & 0 & 0 & -i & 1 & 0 \\ 0 & 0 & i & 0 & i & 0 \\ 0 & 0 & 1 & -i & 0 & 0 \\ -i & -1 & 0 & 0 & 0 & 0 \end{pmatrix} \,, \tag{B20}$$

Decomposing it into spin and orbital parts gives:

$$\begin{aligned} \widetilde{A'} = &\begin{pmatrix} 0 & 0 & i \\ 0 & 0 & 0 \\ -i & 0 & 0 \end{pmatrix} \otimes \sigma^x + \begin{pmatrix} 0 & 0 & 0 \\ 0 & 0 & -i \\ 0 & i & 0 \end{pmatrix} \otimes \sigma^y \\ &+ \begin{pmatrix} 0 & -i & 0 \\ i & 0 & 0 \\ 0 & 0 & 0 \end{pmatrix} \otimes \sigma^z \,. \end{aligned} \tag{B21}$$

Finally, applying this expression to the Hamiltonian (B9) gives [39, 63]:

$$\begin{aligned} \frac{\lambda}{2} \sum_{\mu'\nu'} \widetilde{A'}_{\mu'\nu'} c^\dagger_{\mu'} c_{\nu'} = &\, i\frac{\lambda}{2} c^\dagger_{xz,\alpha} \sigma^x_{\alpha\beta} c_{xy,\beta} + \text{h.c.} \\ &+ i\frac{\lambda}{2} c^\dagger_{xy,\alpha} \sigma^y_{\alpha\beta} c_{yz,\beta} + \text{h.c.} \\ &+ i\frac{\lambda}{2} c^\dagger_{yz,\alpha} \sigma^z_{\alpha\beta} c_{xz,\beta} + \text{h.c.} \,, \end{aligned} \tag{B22}$$

which leads to Eqs. (19)–(21).

Appendix C: Evaluation of Two-loop Diagrams

Diagrams of the two-loop type, as shown in Fig. 4a, can be split into irreducible diagrams. As a result, all two-loop diagrams for a given interaction can be obtained by squaring the sum of irreducible diagrams, as illustrated in Fig. 12.

To illustrate the cancelation of the two diagrams in the sum, we choose the interaction v_{17} and the order parameter $\mathbf{M}_1$. In this case, the sum in the brackets in Fig. 12 is, for the SOC leg related to the Γ spinor:

$$\begin{aligned}
&\frac{\lambda}{2}\sum_{\mathbf{k},n} M_{1,i}\mathrm{tr}[\sigma^z\sigma^i]\mathrm{tr}[\tau^+ G_\Gamma \tau^y G_\Gamma \tilde{\tau}^1 G_X] \\
&\quad +\frac{\lambda}{2}\sum_{\mathbf{k},n} M_{1,i}\mathrm{tr}[\sigma^z\sigma^i]\mathrm{tr}[\tau^- G_X \tilde{\tau}^1 G_\Gamma \tau^y G_\Gamma] \\
=&\lambda\sum_{\mathbf{k},n} M_{1,z}\Big([G_\Gamma\tau^y G_\Gamma]_{21}[G_X]_{11} \\
&\quad +[G_\Gamma\tau^y G_\Gamma]_{12}[G_X]_{11}\Big)\,, \qquad \text{(C1)}
\end{aligned}$$

This term vanishes since $G_\Gamma\tau^y G_\Gamma$ is an antisymmetric matrix. For the contribution from the diagrams with the SOC leg related to the X/Y spinors, we find:

$$\begin{aligned}
&-i\lambda\sum_{\mathbf{k},n}\Big(M_{1,x}\mathrm{tr}\left(\tilde{\tau}^1 G_Y \tau^- G_X \tilde{\tau}^1 G_\Gamma\right) \\
&\quad +M_{1,y}\mathrm{tr}\left(\tilde{\tau}^1 G_Y \tau^+ G_X \tilde{\tau}^1 G_\Gamma\right)\Big) \\
=&-i\lambda\sum_{\mathbf{k},n}\Big(M_{1,x}[G_Y]_{12}[G_X]_{11}[G_\Gamma]_{11} \\
&\quad +M_{1,y}[G_Y]_{11}[G_X]_{21}[G_\Gamma]_{11}\Big)\,, \qquad \text{(C2)}
\end{aligned}$$

which is also zero as the off-diagonal elements of the Green functions G_X and G_Y are odd functions of $\mathbf{k}$. Similar arguments apply in the case when the electron-electron interaction is given by either v_{13}, v_{15} or v_{19} and when the magnetic order parameter is $\mathbf{M}_2$. Thus, all contributions from the two-loop diagrams vanish, and we are left with only the one-loop diagrams shown in Fig. 4b.

Appendix D: Diagrams contributing to w

In this appendix we explain in more details the statement made in the main text concerning the vanishing of the quartic coefficient w in Eq. (38). Let us consider a generic diagram which would contribute to the coefficient w, as shown in Fig. 13.

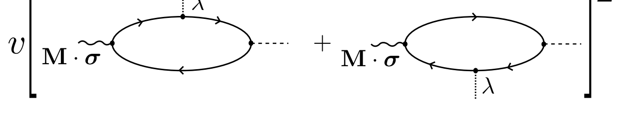

FIG. 12. Illustration of the decomposition of a two-loop diagram into irreducible diagrams.

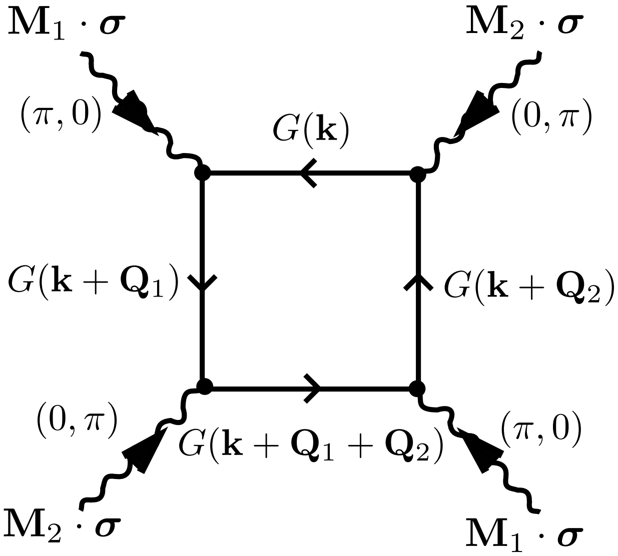

FIG. 13. Illustration of a generic diagram contributing to the coefficient w. Here $\mathbf{Q}_1 = (\pi, 0)$ and $\mathbf{Q}_2 = (0, \pi)$. On the right diagram we have imposed momentum conservation at each vertex, resulting in the appearance of $G(\mathbf{k} + \mathbf{Q}_1 + \mathbf{Q}_2)$.

Note that we do not specify any vertices, i.e. the coupling between the electrons and the SDW order parameters do not necessarily arise from Eq. 28. Due to the Pauli matrix contraction, the diagram must have alternating $\mathbf{M}_1$ and $\mathbf{M}_2$ legs in order for it to contribute to w. Indeed, performing the trace over spin indices gives:

$$M_1^i M_2^j M_1^k M_2^l \;\mathrm{tr}\left(\sigma^i\sigma^j\sigma^k\sigma^l\right)\,. \qquad \text{(D1)}$$

Using Eq. 31, we find:

$$2\left(\mathbf{M}_1\cdot\mathbf{M}_2\right)^2 - \mathbf{M}_1^2\mathbf{M}_2^2\,, \qquad \text{(D2)}$$

thus resulting in a $\left(\mathbf{M}_1\cdot\mathbf{M}_2\right)^2$ term. This contrasts to the third diagram in Fig. 9, which gives no contribution of the form $\left(\mathbf{M}_1\cdot\mathbf{M}_2\right)^2$ after tracing over the Pauli matrices.

Let us now consider the internal lines of the diagram. Since $\mathbf{M}_1$ carries momentum $(\pi, 0)$ and $\mathbf{M}_2$ carries momentum $(0, \pi)$, the only way for momentum to be conserved is if one of the lines corresponds to a propagator with momentum $\mathbf{Q}_1 + \mathbf{Q}_2 = (\pi, \pi)$. However, in the absence of a Fermi pocket at $M = (\pi, \pi)$ (of the unfolded Brillouin zone), this will be an off-shell contribution. Thus, contributions to w must arise from the electronic states near $M = (\pi, \pi)$.